

Vortex impingement onto an axisymmetric obstacle – subcritical bifurcation to vortex breakdown

S. Pasche^{1,†}, F. Avellan² and F. Gallaire³

¹Linné FLOW centre, Department of Mechanics, KTH, SE-100 44 Stockholm, Sweden

²Laboratory for Hydraulic Machines, Ecole Polytechnique Fédérale de Lausanne, CH-1007 Lausanne, Switzerland

³Laboratory of Fluid Mechanics and Instabilities, Ecole Polytechnique Fédérale de Lausanne, CH-1015 Lausanne, Switzerland

(Received 15 December 2019; revised 30 August 2020; accepted 10 November 2020)

A swirling wake flow submitted to an adverse pressure gradient is studied by bifurcation analysis, modal analysis and direct numerical simulations. In contrast to experiments in diverging tubes, the adverse pressure gradient is imposed by the presence of a downstream axisymmetric obstacle centred on the vortex axis. Different adverse pressure gradients are investigated by modifying the obstacle radius, which results in the deceleration of the vortex axial velocity. Hence, vortex breakdown occurs for a sufficiently large pressure gradient. We observe a spiral vortex breakdown type without any recirculation bubble, which contrasts with classical spiral vortex breakdown developing in the bubble wake. A weakly nonlinear analysis is performed to characterize this self-sustained instability. The resulting Landau equation reveals the sub-critical character of this Hopf bifurcation, highlighting a sub-critical vortex breakdown. In addition, the stabilization mechanism of this spiral vortex breakdown caused by an off-centre displacement of the downstream axisymmetric obstacle is investigated by direct numerical simulations. Nonlinear dynamics, such as a quasi-periodic state, is observed as a consequence of nonlinear interactions between the spiral vortex breakdown and the misalignment of the obstacle before the stabilization occurs.

Key words: vortex breakdown, flow–structure interactions

1. Introduction

Vortex breakdown is a hydrodynamic phenomenon that affects swirling jet and wake flows. It is commonly defined as an abrupt change of the flow topology going from a columnar

† Email address for correspondence: simon.pasche@alumni.epfl.ch

vortex state to one of the possible vortex breakdown states, which are characterized by a backward flow reversal along the vortex axis (Shtern & Hussain 1999; Lucca-Negro & O'Doherty 2001). These breakdown states are the bubble vortex breakdown, the spiral vortex breakdown or the multiple helical vortex breakdown. This transition is mainly controlled by two parameters, the Reynolds number, and the Swirl number, the latter typically defined as the ratio between the maximum azimuthal velocity and the centreline axial velocity. Several swirling flows in industrial applications undergo vortex breakdown. While it ensures flame stabilization and enhances mixing in combustion chambers (Paschereit, Flohr & Gutmark 2002; Oberleithner *et al.* 2015), it causes in contrast manoeuvrability difficulties of delta wings as it may cause unsteady fluctuations (Lambourne & Bryer 1962). Such unsteady fluctuations can also jeopardize the mechanical structure of hydraulic turbomachinery operating at off-design conditions due to unsteady loading and fatigue (Pasche, Gallaire & Avellan 2019).

Over the years, vortex breakdown has been investigated in several configurations and for a wide range of swirl and Reynolds numbers (see Hall 1972; Leibovich 1978; Lucca-Negro & O'Doherty 2001). Closed container experiments with a rotating end wall produce vortex breakdown into a steady recirculation bubble at a constant streamwise position, among other vortex breakdown types. This configuration is particularly convenient to perform experimental measurements and numerical simulations to explore vortex breakdown topology (Escudier 1984; Spohn, Moiry & Hopfinger 1993; Serre & Bontoux 2002). Recently, the circular geometry has been substituted by a polygonal container introducing boundary effects and modifying the bifurcation map of the vortex breakdown (Naumov & Podolskaya 2017). Swirling jet flows in open tubes have also been thoroughly studied. Flow maps portraying the vortex breakdown type as a function of the breakdown location, Reynolds number and swirl number have been reported by Sarpkaya (1971). Spiral vortex breakdown is observed at smaller swirl and Reynolds numbers than the bubble vortex breakdown, which is observed at larger swirl and Reynolds numbers. At even larger swirl, multiple helical vortex breakdown has also been observed (see Alekseenko *et al.* 1999; Okulov 2004; Sorensen, Naumov & Okulov 2011). Two- and three-dimensional direct numerical simulations of canonical vortices, such as the Batchelor, Grabowski and Berger or Maxworthy vortex profiles, have contributed to the further understanding of vortex breakdown by investigating the effect of confinement, the resulting bifurcation diagrams and possible route to chaos (see Althaus *et al.* 1994; Sotiropoulos, Ventikos & Lackey 2001; Mattner, Joubert & Chong 2002; Ruith *et al.* 2003; Jochmann *et al.* 2006; Jones, Hourigan & Thompson 2015; Pasche, Gallaire & Avellan 2018*b*; Moise & Mathew 2019), among others.

The formation of the recirculation follows two possible scenarios: along the first scenario, the bubble can develop from a smooth transition as the bifurcation parameter (swirl or Reynolds number) increases. The axial velocity, which is initially positive, diminishes progressively until it changes sign and becomes negative, forming the recirculation bubble. This transition has been observed in closed containers and open configurations for a Grabowsky and Berger vortex profile prevailing at the inlet (see Ruith *et al.* 2003; Meliga, Gallaire & Chomaz 2012; Viola 2016). In the second scenario, the bubble is formed through a saddle-node bifurcation, inducing a sudden transition to a recirculation flow. This transition is illustrated in Lopez (1994) for low Reynolds number flow. In the latter case, a Batchelor vortex is considered at the inlet of an open pipe, where the bubble vortex breakdown is induced by a small contraction of the pipe. A similar bifurcation structure has been theoretically and numerically predicted in the inviscid limit (see Wang & Rusak 1997; Rusak, Whiting &

Wang 1998). In this second scenario, a hysteresis region appears where both columnar and bubble vortex breakdown solutions coexist for bifurcation parameters above a certain threshold.

Regarding the spiral vortex breakdown state, the most commonly acknowledged interpretation relies on a secondary destabilization of an helical disturbance that feeds on an axisymmetric recirculation bubble that prevails at early stages (see Ruith *et al.* 2003; Herrada & Fernandez-Feria 2006). The formation of the spiral has been identified as resulting from the absolutely unstable nature of a helical mode in the wake of the vortex breakdown bubble (see Gallaire *et al.* 2006). This secondary destabilization can also be characterized by a global stability analysis, which reveals a wavemaker also located in the recirculation bubble wake (Meliga *et al.* 2012; Qadri, Mistry & Juniper 2013). In this unbounded flow, this helical instability results in a supercritical Hopf bifurcation leading to a limit cycle solution with the spiral winding around the recirculation bubble. It should be also noted that in some other flow configurations, in particular in the presence of centrifugally unstable inlet velocity profiles, for instance in the experiment by Billant, Chomaz & Huerre (1998), the appearance of double helical ($m = 2$) and triple helical ($m = 3$) modes precedes the appearance of recirculation bubbles. These helical pre-breakdown states were interpreted as primary absolute instabilities by Gallaire & Chomaz (2003).

Besides an increase in swirl or Reynolds numbers, vortex breakdown can be favoured by a divergent pipe, as first used in the experimental study of Sarpkaya (1971). It has been shown that the greater the divergence of the pipe, or the adverse pressure gradient, the less swirl is needed to generate breakdown (see Sarpkaya 1974; Krause 1985; Pagan & Benay 1987; Spall, Gatski & Ash 1990). The role of divergent pipes on the bifurcation structure associated with axisymmetric vortex breakdown has also been investigated theoretically in the inviscid limit by Rusak *et al.* (2017), Rusak, Judd & Wang (1997) and Wang & Rusak (1997). In addition to the diverging pipe, a second configuration has been investigated: a free vortex entering an air intake whose mass flow can be varied by an adjustable contraction (see Delery 1994). By reducing the mass flow, an adverse pressure gradient was imposed on the incoming vortex provoking vortex breakdown. A similar flow configuration has been recently investigated by Pasche *et al.* (2014), where the adverse pressure gradient was generated by a sphere, which results in a single spiral mode without a recirculation bubble. Such a configuration has been rarely studied despite its relevance for vortex structure interactions, a subject for instance reviewed by Rockwell (1998).

In the present study, we perform a numerical study inspired by the experimental investigation of Pasche *et al.* (2014). The dynamics of the streamwise impinging of the Batchelor vortex onto an axisymmetric obstacle is investigated for laminar flow conditions. The spherical obstacle investigated in the former paper is replaced by an axisymmetric obstacle to avoid purposeless numerical complexities due to the sphere wake. The two-dimensional (2-D) axisymmetric steady Navier–Stokes equations are first solved and we perform a bifurcation analysis on the aspect ratio, swirl number and Reynolds number. These results are supported by three-dimensional (3-D) direct numerical flow simulations (DNS) for specific bifurcation parameters. The present study focuses on the development of a single spiral mode of vortex breakdown as observed by Lambourne & Bryer (1962) and Pagan & Benay (1987). In addition, the dynamics of the vortex streamwise impingement in a presence of a misalignment between the vortex centre and the obstacle axis is investigated. Even a small displacement leads to a stable vortex and the route to this stabilization is investigated using bifurcation theory.

2. Configuration

We investigate numerically the streamwise impingement of a canonical Batchelor vortex onto an elongated axisymmetric obstacle. A cylindrical coordinate system (R, θ, Z) is introduced, whose axial component is aligned along the obstacle centreline. In this coordinate system, the fluid motion, associated with the state vector $\mathbf{q} = (U_R, U_\theta, U_Z, P)$, is governed by the Navier–Stokes equations and characterized by a homogeneous and incompressible fluid of kinematic viscosity ν . The variables are scaled by the physical length and velocities defined as the vortex core size R_v and a uniform axial velocity U_∞ at the inlet, respectively. These reference scales refer to the upstream vortex defined as a Batchelor vortex, which writes in dimensionless variables

$$U_R(R) = 0, \quad U_\theta(R) = S \frac{(1 - e^{-R^2})}{R}, \quad U_Z(R) = 1, \quad \text{on } \Gamma_{in}, \quad (2.1)$$

where S is the swirl number defined as $S = R_v \Omega_0 / U_\infty$ with Ω_0 the vorticity and R_v the radius of the vortex. Using this scaling, the dimensionless Navier–Stokes equations writes in vector formulation as

$$\left. \begin{aligned} \frac{\partial \mathbf{U}}{\partial t} + (\mathbf{U} \cdot \nabla) \mathbf{U} &= -\nabla P + Re^{-1} \nabla^2 \mathbf{U}, & \text{in } \Omega, \\ \nabla \cdot \mathbf{U} &= 0, & \text{in } \Omega, \end{aligned} \right\} \quad (2.2)$$

with the Reynolds number defined as $Re = R_v U_\infty / \nu$. We solve these equations in a large computational domain $R_{max} = 10R_s$ and $Z_{free} = 19R_s$, where R_s is the obstacle radius. These conditions ensure the vortex in front of the obstacle to be free of inlet and radial disturbances, by isolating the vortex from the free outflow condition imposed on the external boundary Γ_{ext} (see Pasche *et al.* 2018b). The Batchelor vortex, (2.1), is imposed at the inlet $Z = 0$ and can be aligned or shifted by an offset D regarding the obstacle axis. The obstacle extends up to the outlet boundary Γ_{out} to avoid flow unsteadiness due to the wake of the obstacle. The Navier–Stokes equations are solved in a 2-D axisymmetric domain and in a 3-D domain. In the 2-D axisymmetric domain, a free outflow $((-PI + Re^{-1} \cdot (\nabla V)) \cdot \mathbf{n} = 0)$ is imposed on the outlet boundary Γ_{out} , while in the 3-D domain, a convective boundary condition is imposed on Γ_{out} ($\partial_t V + U_c \cdot \partial_n V = 0$). We fix the convective velocity to be equal to the free-stream velocity $U_c = (0, 0, 1)$. This change of the outlet boundary condition does not impact the flow dynamics as it is imposed far away from the obstacle nose $Z_{obs} = 10R_s$.

In this configuration, the obstacle that the vortex must accommodate is defined by a swirl profile radius ratio, in short aspect ratio $h = R_v / R_s$. The different parameters investigated are summarized in table 1. We consider only obstacles that have a larger radius than the vortex core inducing a strong topology change of the vortex. The adverse pressure gradient modifies both the viscous core and the potential vortex region to force the deflection of the vortex circumventing the obstacle.

We introduce a second non-dimensional length scale $\tilde{Z} = Z \times h$ and $\tilde{R} = R \times h$, which is more appropriate to portray the flow solution because it enables a generalized representation of the computational domain for any aspect ratio studied. Thus, in the figures of the present study, the obstacle radius becomes unity and the vortex core size adjusts consequently. Any variables specified with $(\tilde{\cdot})$ use the newly introduced length scale, which is just a rescaling factor.

Description	$h = R_v/R_s$	S	Re	D
2-D axi	0.5	0.85–1.2	0–1200	—
2-D axi	0.25	0.85–1.2	0–1500	—
3-D	0.5	1.0	312–324.5	—
3-D	0.25	1.0	212.5–225	—
3-D	0.25	1.0	224.75	0.0–0.2

Table 1. Parameters of the present numerical analysis, h the aspect ratio between half the vortex core size and the obstacle radius, S the swirl number, Re the Reynolds number based on the vortex and D the lateral displacement of the vortex.

3. Methods of analysis

We consider both 2-D axisymmetric configuration and 3-D configuration of the computational domain. The 2-D axisymmetric analysis allows us to perform bifurcation, modal and weakly nonlinear (WNL) analysis. The 3-D DNS analysis validates the 2-D axisymmetric simulations and provides a deeper understanding of symmetry breaking of the flow when the vortex is laterally displaced.

3.1. Two-dimensional axisymmetric analysis

We look for laminar solutions of the flow by solving the 2-D axisymmetric steady Navier–Stokes equations for a wide range of Reynolds numbers and swirl numbers. These solutions are explored by performing a bifurcation analysis on the Reynolds number for several specified swirl numbers. An arc-length continuation method is used to follow the stable and unstable branches of the base flow. As an axisymmetric coordinate system is used, critical points in the space of the bifurcation parameters can be associated with different azimuthal wavenumbers m . The boundaries of these critical points are tracked using a fold tracking algorithm and a Hopf tracking algorithm (Salinger *et al.* 2005), for the azimuthal wavenumber $m = 0$ and $m = 1$, respectively. The higher azimuthal wavenumbers are not tracked in the present study because the azimuthal wavenumber $m = 2$ becomes dominant for high swirl number, as already observed in Sarpkaya (1974) and Meliga *et al.* (2012). The results of a convergence study are presented in appendix A. These modes are highlighted in the modal analysis too. Linear global stability analysis is performed (see Pasche *et al.* (2018b) for details and validation), which allows us to access the full spectrum of the flow while tracking algorithms follow the marginally unstable eigenmode of specific azimuthal wavenumbers.

In the linear global stability analysis, the flow is decomposed into a base flow q_0 and a disturbance q' . The disturbance q' is expanded in normal modes for different azimuthal wavenumbers $m \in \mathbb{Z}$,

$$q'(R, \theta, Z, t) = q_1(R, Z) \exp(-i\omega t + im\theta) + \text{c.c.}, \tag{3.1}$$

where c.c. is the complex conjugate. The substitution of this definition in the governing equations (2.2), leads to an eigenvalue equation expressed in a compact form as

$$((\omega_i - i\omega_r)\mathcal{N} + \mathcal{L}_m(U)) q_1 = \mathbf{0}, \quad \text{in } \Omega_a, \tag{3.2}$$

where \mathcal{L}_m is the operator for the linearized Navier–Stokes equations of azimuthal wavenumber m . This eigenvalue problem results in eigenvalues and eigenmodes that will lead to self-sustained instability for unstable cases. This problem is solved using the finite element library FreeFem++ (Hecht 2012), see appendix B.

3.2. Weakly nonlinear analysis

A multiple time scale analysis is performed at the critical Reynolds value Re_c , of the marginally unstable eigenmode \mathbf{q}_1 of eigenvalue $-i\omega_c$, to investigate the WNL mechanism behind the flow bifurcations. An asymptotic expansion of the flow field $\mathbf{q} = (U_R, U_\theta, U_Z, P)$ regarding the small parameter ϵ is considered

$$\mathbf{q} = \mathbf{q}_0 + \epsilon \mathbf{q}_1 + \epsilon^2 \mathbf{q}_2 + \epsilon^3 \mathbf{q}_3 + \text{h.o.t.}, \quad (3.3)$$

where h.o.t stands for higher-order terms, and where $0 < \epsilon \ll 1$ and defines the distance from the thresholds (3.4). In addition, we assume that the Reynolds number departs from criticality at order ϵ^2 , yielding

$$\frac{1}{Re} = \frac{1}{Re_c} - \epsilon^2. \quad (3.4)$$

The unsteady dynamics is decomposed into a fast time scale t_0 and slow time scale T_{2i} , the latter start acting at ϵ^2 too:

$$t = t_0 + \sum_{i \geq 1} \epsilon^{2i} T_{2i}. \quad (3.5)$$

This scaling has been used for axisymmetric flows (see Meliga *et al.* 2012; Citro *et al.* 2016). Substituting the asymptotic expansion, (3.3) in the governing equations (2.2) and using the chain rule for the derivative involving multiple time scales results in systems of equations at different epsilon orders that are solved. These equations are summarized in appendix B and the reader is invited to read Meliga *et al.* (2012) and Sipp & Lebedev (2007) for additional explanations.

The WNL analysis leads to the definition of an amplitude equation that describes slow modulation in time and space of patterns out of equilibrium. This approach is only valid for WNL conditions, which means close to the threshold of instability $Re \approx Re_c$, and provides only qualitative results in the stronger nonlinear regime. Nevertheless, the amplitude equation describes completely the pattern forming in its range of validity. In the present case, we will show that the flow dynamics follows a Landau amplitude equation, which writes, up to the fifth order (see Fujimura 1991; Dusek, Gal & Fraunié 1994),

$$\frac{\partial a}{\partial t} - \epsilon^2(\lambda_1 + \epsilon^2 \lambda_2)a - (\mu_1 + \epsilon^2 \mu_2)a|a|^2 - \gamma a|a|^4 = 0, \quad (3.6)$$

with λ , μ and γ complex coefficients and a the complex amplitude.

The amplitude a , solution of (3.6), allows a direct comparison to DNS results when the energy norm of the eigenvector matches the energy of the DNS disturbance. The DNS solution is a real value velocity field and the WNL analysis is performed in the complex number set. Thus, only half the energy of the WNL analysis has to be used to compare with the DNS, i.e. the complex conjugate part of the product is dropped. The final solution of the WNL analysis writes

$$\begin{aligned} \mathbf{q} = & \mathbf{q}_0 + a \mathbf{q}_{1a} \exp(i\theta - i\omega_c t) + |a|^2 \mathbf{q}_{3a|a|^2} \exp(i\theta - i\omega_c t) \\ & + |a|^4 \mathbf{q}_{5a|a|^4} \exp(i\theta - i\omega_c t) + \text{h.o.t} + \text{c.c.} \end{aligned} \quad (3.7)$$

Assuming the decomposition: $a = \rho(t) e^{i\phi(t)}$, the following equation holds for the disturbance amplitude:

$$\sqrt{(\mathbf{q} - \mathbf{q}_0)^2} = \sqrt{\rho \rho^* (e^{i\phi} \mathbf{q}_{1a} e^{i\theta - i\omega_c t}, e^{-i\phi} \mathbf{q}_{1a}^* e^{-i\theta + i\omega_c t})} + \text{h.o.t.}, \quad (3.8)$$

Vortex impingement onto an axisymmetric obstacle

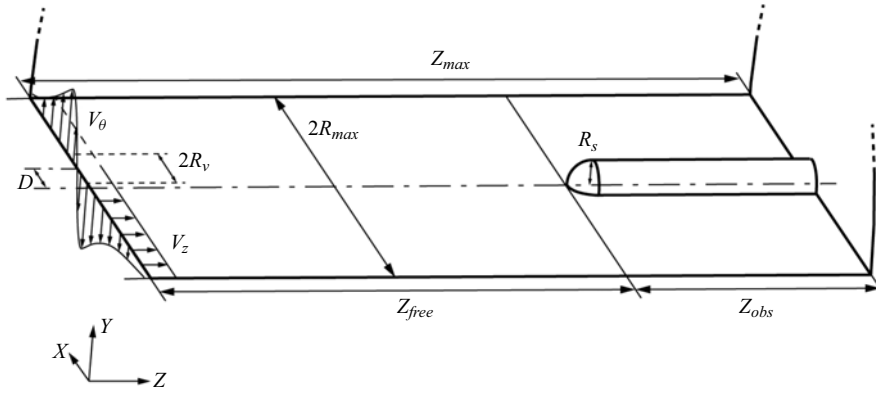


Figure 1. Half of the computational domain.

where the left-hand side is the disturbance amplitude of the DNS and the right-hand side is the disturbance amplitude of the WNL analysis. It results in

$$\sqrt{(\mathbf{q} - \mathbf{q}_0)^2} = \sqrt{\rho\rho^* + \rho\rho^*|\rho|^2} + \text{h.o.t} \quad (3.9)$$

using the following normalization of the adjoint eigenmode:

$$(\mathbf{q}_{1a}, \mathbf{q}_{1a}^*) = \int_{\Omega} \mathbf{q}_{1a} \cdot \mathbf{q}_{1a}^* = 1, \quad (3.10)$$

which approximates very well the nonlinear disturbance amplitude at threshold. However, it can differ further away from the threshold because of nonlinear interactions. Once again, the computation of the WNL expansion is performed using the FreeFem++ library, involving the resolution of eigenvalue, adjoint eigenvalue and resolvent problems, which are expressed in [appendix B](#).

3.3. Three-dimensional direct numerical flow simulations

Direct numerical flow simulations of the configuration displayed in [figure 1](#) have been performed using NEK5000, a spectral element solver developed by Fischer, Lottes & Kerkemeier (2008). An O-grid mesh is used to mesh the obstacle. We use a convective boundary condition at the outlet that avoids backward waves and helps convergence for this swirling flow. Similar simulations of the vortex breakdown have already been performed by the authors in Pasche *et al.* (2018b). A convergence analysis is presented in [appendix A](#).

4. Bifurcation analysis

Let us start by introducing an axisymmetric flow solution for $S = 1.05$ and $Re = 255.5$ with and without a downstream obstacle having an aspect ratio of $h = 0.5$, see [figure 2](#). The flows are illustrated by surface streamlines coloured by the axial velocity magnitude on the upward R coordinate and by the azimuthal velocity magnitude on the downward R coordinate. In [figure 2\(a\)](#), the flow is purely columnar and the vortex progressively dissipates by viscous diffusion as it propagates downstream. On the contrary, the formation of a recirculation bubble is observed when an obstacle is located on the vortex trajectory for the parameters considered. This obstacle generates an adverse pressure gradient which

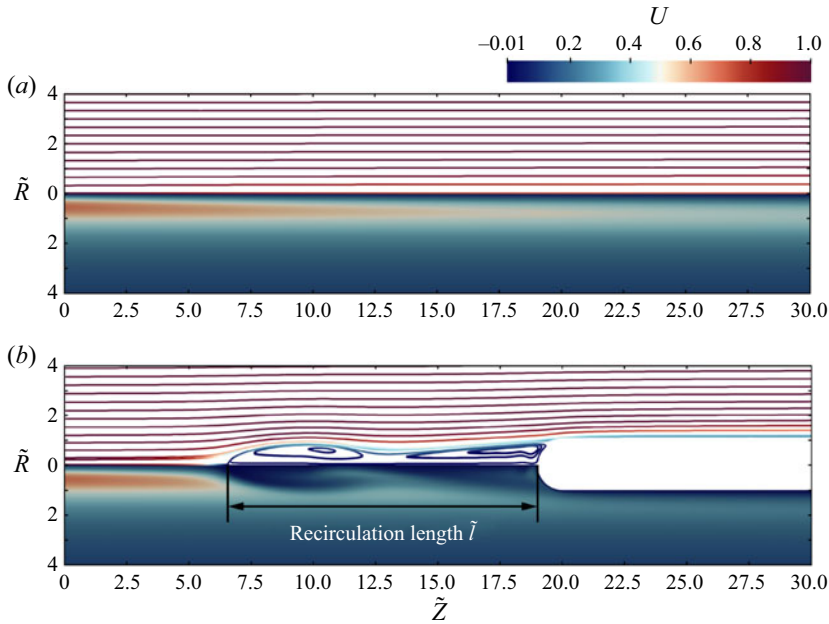


Figure 2. Two-dimensional axisymmetric vortex flow solutions at $S = 1.05$, $Re = 255.5$ without impingement (a), and with impingement onto a downstream obstacle $h = 0.5$ (b). On the upward R coordinate, the figure shows surface streamlines coloured by the axial velocity magnitude, and on the downward R coordinate the figure shows the azimuthal velocity component. Both examples are stable solutions. Panel (b) represents a typical solution observed in the present numerical study.

originates in this change of flow topology. The recirculation bubble is reminiscent of a bubble vortex breakdown, which is characterized by a negative velocity on the axis defining the starting location of the bubble (see Leibovich & Stewartson 1983). Behind the first vortex breakdown bubble, a typical swirling wake flow develops, which attaches to the obstacle, generating a second recirculation region.

The adverse pressure gradient decelerates mainly the axial velocity on the centreline, while the azimuthal velocity remains almost constant before the vortex breaks down (see Delery 1994; Pasche *et al.* 2014). In an axisymmetric system, the azimuthal velocity is mainly affected by the radial momentum through the radial pressure gradient. The transport of the azimuthal momentum is ensured by nonlinear advection. In contrast, the axial pressure gradient modifies straightforwardly the axial momentum. Thus, the axial velocity is first decelerated, and then the azimuthal velocity is modified as the recirculation bubble is reached.

In figure 2(b), we define the recirculation length, which measures the length between the obstacle front and the upstream zero value of the axial velocity on the axis. This recirculation length is used, in the present study, as a bifurcation parameter to identify the different bifurcation branches of the flow. The associated bifurcation diagrams are presented for two configurations: an aspect ratio $h = 0.5$ in figure 3(a) and an aspect ratio $h = 0.25$ in figure 3(b). The black curves, which represent bifurcation branches, show the recirculation length of the bubble on the vertical axis as a function of the Reynolds number Re , for different values of the swirl number S . As the Reynolds number is increased, the recirculation bubble propagates upstream, following a cusp shape in the bifurcation diagram. Such a transition is similar to the saddle-node bifurcation observed

Vortex impingement onto an axisymmetric obstacle

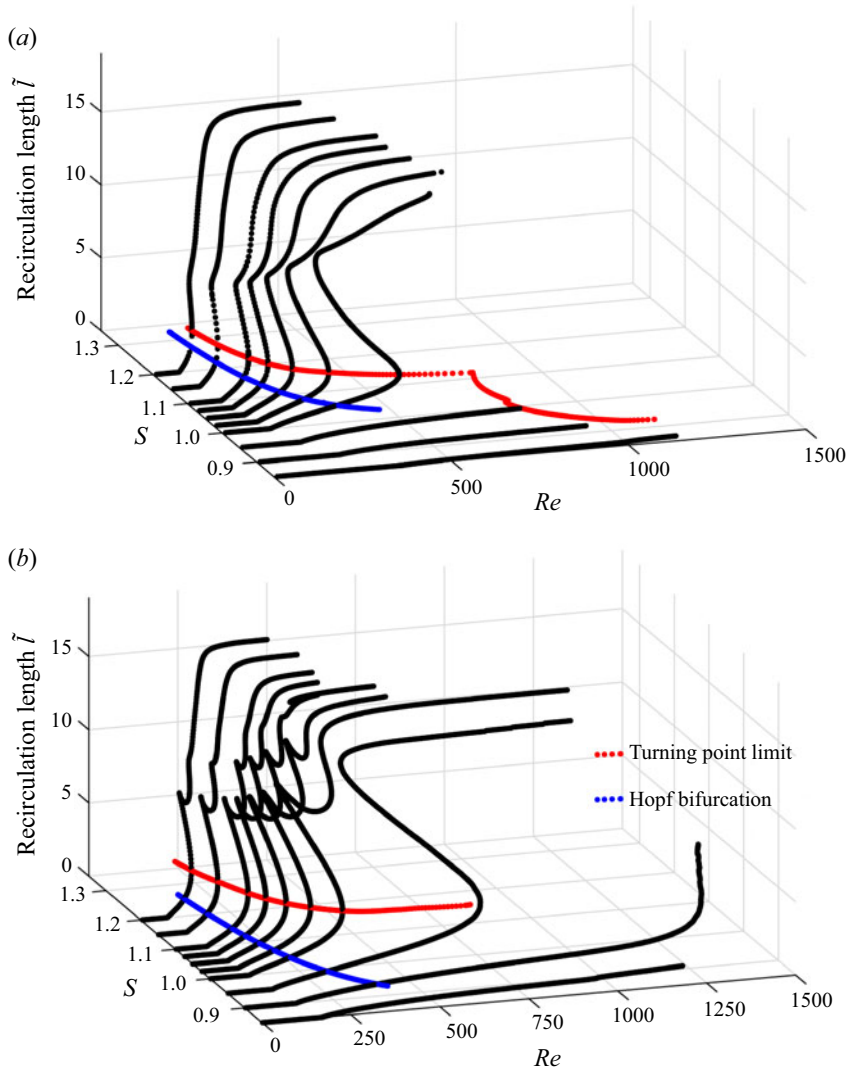


Figure 3. Axisymmetric bifurcation map of the vortex impinging a downstream obstacle for two aspect ratios; $h = 0.5$ (a) and $h = 0.25$ (b). The red dots show the saddle-node bifurcation threshold, and the blue dots show the Hopf bifurcation threshold.

by Lopez (1994) resulting from the presence of a radial contraction in a numerical tube experiment. In figure 3, the forward branches represent stable solutions, while the backward branches represent unstable solutions. For $h = 0.5$, the transition is smooth, while for $h = 0.25$ several unstable branches appear, increasing the complexity of the bifurcation diagram. In both cases, as the swirl number is increased, the first bifurcation appears at smaller Reynolds numbers and the cusp shapes are damped, tending to the bubble vortex breakdown solution of the canonical vortex observed in tube experiments (see Meliga & Gallaire 2011). At lower Reynolds number, we observe in figure 3 that the bifurcation curves are flat, implying that the flow is attached to the obstacle. On the contrary, at the largest displayed Reynolds numbers, the recirculation lengths remain constant because the back flow approaches the inlet of the computational domain. A larger

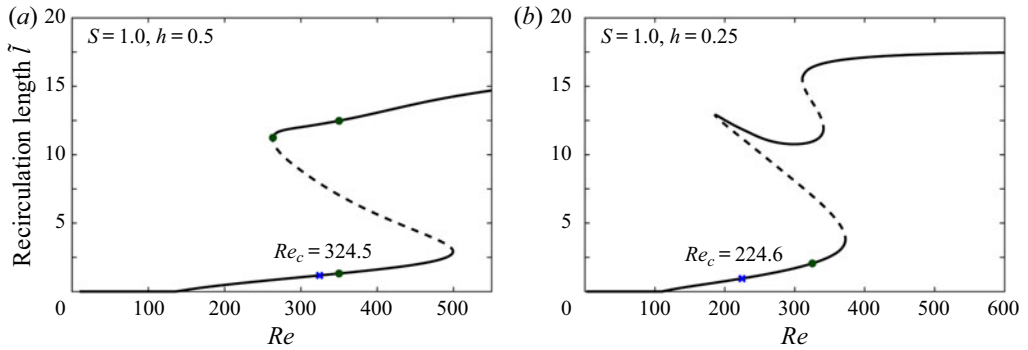


Figure 4. Bifurcation curves of the axisymmetric vortex flow impinging an obstacle of aspect ratio $h = R_v/R_s = 0.5$ (a) and $h = 0.25$ (b), for a swirl number of $S = 1.0$. The dashed curves represent the unstable branch, while the solid curves represent the stable branches. The blue crosses exhibit the critical Reynolds number Re_c of the Hopf bifurcation, and the green dots exhibit the selected bifurcation points represented in the subsequent figures 5 and 6.

obstacle size shifts the saddle-node bifurcation to smaller Reynolds number as already reported by Delery (1994) and Pasche *et al.* (2014).

In figure 3, we also present the outcome of the turning point and the Hopf point tracking algorithms. The red dots are the neutrally stable limit of the flow for the azimuthal wavenumber $m = 0$. These curves accurately fall on the stable–unstable limit of the bifurcation branches, which has already been observed for swirling flows (Meliga & Gallaire 2011; Pasche, Avellan & Gallaire 2018a). The blue dots represent the neutrally stable limit of the flow concerning the azimuthal wavenumber $m = 1$, i.e. limit cycle solutions.

The detailed bifurcation curves for a $S = 1.0$ are shown in figure 4. The unstable branches are represented by discontinuous curves and the solid lines represent stable branches. The critical Reynolds number at which the Hopf bifurcation occurs is indicated with blue crosses. In both cases, the turning points giving birth to the second stable branches appear before the critical Reynolds number of the Hopf bifurcation.

The flow solutions of the first and second stable branches are illustrated in figure 5, and correspond to the bifurcation parameters of the green dots in figure 4. On the first stable branch, at low Reynolds number, the classical stagnation point is recovered. As the Reynolds number increases, a small recirculation region is observed in front of the obstacle as illustrated in figure 5(a) at $Re = 350$, $S = 1.0$ and $h = 0.5$. This recirculation slowly propagates upstream until the turning point is reached, and remains attached to the obstacle. On the unstable branch, the recirculation zone increases without the formation of a separate bubble, to merge with the first axisymmetric solution on the second stable branch, see the turning point in figure 5(b) at $Re = 263.2$ and $S = 1.0$. Then, the recirculation zone separates from the obstacle and defines a detached bubble as illustrated in figure 5(c) at $Re = 350$ and $S = 1.0$ (note the relative analogy with the upper branch solution depicted in figure 2(b) for $S = 1.05$ and $Re = 255.5$). The transition from the attached to the detached recirculation bubble occurs smoothly as the Reynolds number increases. The second stable branch is, therefore, associated with the development of the bubble vortex breakdown. Regarding the smaller aspect ratio $h = 0.25$, whose first stable branch solution is displayed in figure 5(d) at $Re = 325.1$ and $S = 1.0$, a similar scenario is observed up to the second stable branch: the recirculation bubble detaches from the

Vortex impingement onto an axisymmetric obstacle

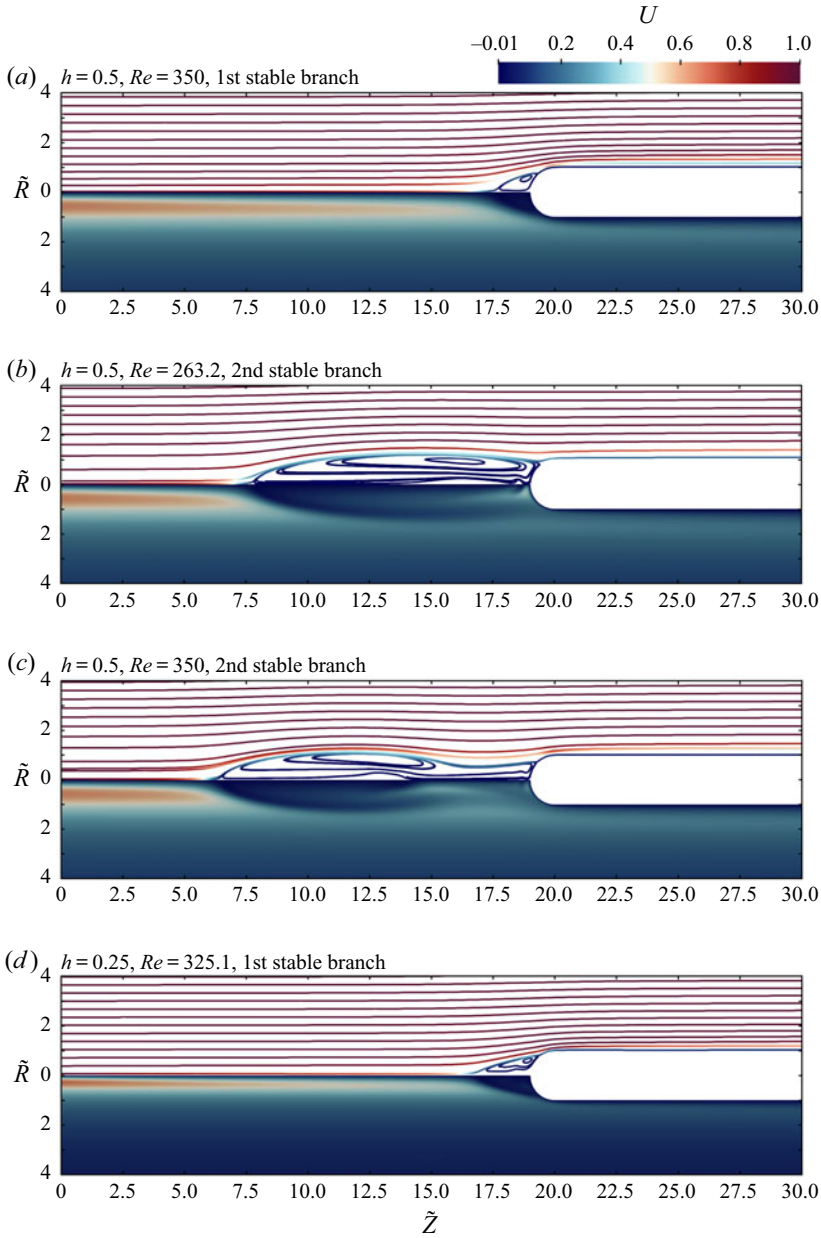


Figure 5. Axisymmetric vortex flow solutions for $h = 0.5$ and $S = 1.0$, on the first stable branch $Re = 350.0$ (a), at the threshold of the second stable branch $Re = 263.2$ (b) and on the second stable branch $Re = 350$ (c), as well as the solution for $h = 0.25$ and $S = 1.0$ on the first stable branch $Re = 325.1$ (d). These solutions correspond to the green dots in figure 4.

obstacle and moves upstream letting a second recirculation region appear, which remains attached to the obstacle.

Moreover, we present the eigenvalue spectra of the solutions corresponding to the green dots displayed in figures 4 and 5. On the first stable axisymmetric branch at $h = 0.5$ and $Re = 350$ (see figure 6a) the eigenvalue spectrum displays an unstable eigenvalue of

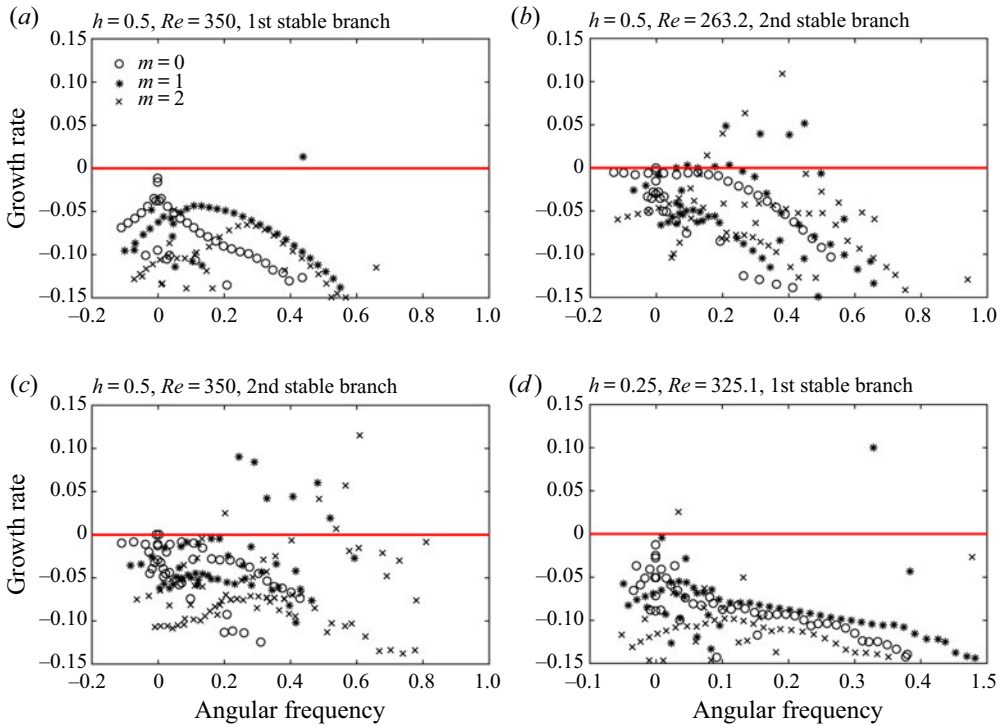


Figure 6. Eigenvalue spectra of the axisymmetric vortex solution $h = 0.5, S = 1.0$ for the first stable branch at $Re = 350.0$ (a), for the second stable branch at $Re = 263.2$ (b) and for the second stable branch at $Re = 350$ (c), as well as the first stable branch for $h = 0.25, S = 1, Re = 325.1$ (d). These solutions correspond to the green dots in figure 4.

azimuthal wavenumber $m = 1$. This eigenvalue growth rate is positive in agreement with the critical Reynolds number at $Re_c = 324.5$ of the Hopf tracking method. The eigenvalue spectrum at $h = 0.5$ and $Re = 263.2$ for the second stable branch displays several unstable eigenvalues of azimuthal wavenumber $m = 1$ and $m = 2$ showing the hydrodynamically unstable flow field (figure 6b). As we move along the second stable branch, the number of unstable eigenmodes increases and their growth rates are strengthened (figure 6c). The eigenvalue spectrum at $h = 0.25$ displays two unstable eigenvalues on the first stable branch: a first unstable eigenmode of azimuthal wavenumber $m = 1$ and a second of $m = 2$, see figure 6(d). The latter has a smaller growth rate and a lower frequency than the unstable mode $m = 1$. We observe on the eigenvector plot (not shown here) that the second unstable mode develops in the recirculation region in front of the obstacle while the first unstable mode is the helical unstable mode of the spiral vortex breakdown.

We observe, finally, that in contrast to the saddle-node bifurcation of Lopez (2006), the second stable axisymmetric branch of a vortex impinging an obstacle is strongly unstable and cannot exist in 3-D configurations. Only the first axisymmetric stable branch can exist. While the Reynolds or swirl numbers are increased, a recirculation zone ahead of the obstacle develops, which is submitted to a Hopf bifurcation of azimuthal wavenumber $m = 1$ as a first instability.

Vortex impingement onto an axisymmetric obstacle

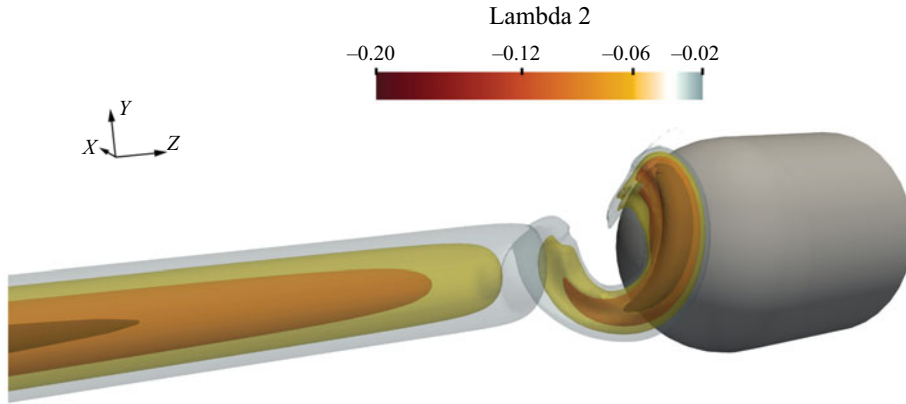


Figure 7. Axial vorticity of the 3-D solution for $S = 1.0$, $Re = 224.6$ and $h = 0.25$.

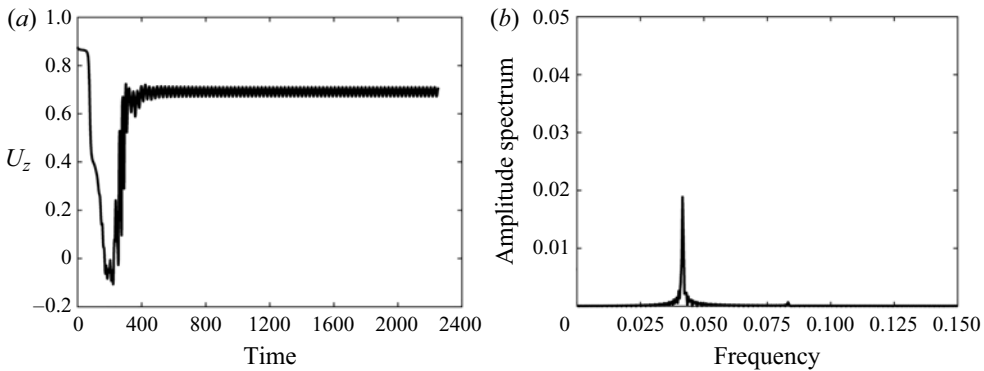


Figure 8. Time series (a) and amplitude Fourier spectrum (b) of the 3-D DNSs at $(\tilde{X}, \tilde{Y}, \tilde{Z}) = (0.5, 0.0, 18.0)$ for the axial velocity and $S = 1.0$ and $h = 0.25$, and for $Re = 218.75$ (a,b), respectively.

5. Subcritical Hopf bifurcation

The flow, issued from the 3-D direct numerical flow simulations, is illustrated by the lambda 2 criterion in [figure 7](#) for $h = 0.25$ and $S = 1.0$. The development of a single helical spiral in front of the obstacle is shown. This mode is also obtained in the 2-D axisymmetric solution represented by the eigenmode of the most unstable eigenvalue having the same winding direction and temporal rotation as the 3-D solution. In addition, the spiral suddenly forms from the centreline of the vortex without the development of a recirculation bubble. Such a spiral vortex breakdown has the same origin as the single spiral appearing in the wake of a recirculation bubble, (see [Gallaire et al. 2006](#)). Both are hydrodynamic instabilities of a swirling wake flow.

The time series of the flow and the Fourier amplitude spectrum of this 3-D solution is portrayed in [figure 8](#). A limit cycle solution is observed with a well-defined frequency. However, the periodic solution displayed in [figure 8](#) at $Re = 218.75$ appears for a smaller Reynolds number than the critical Reynolds number $Re = 224.6$ identified by modal analysis. This shift is not a numerical inaccuracy. The transition from a steady to an unsteady dynamics of the vortex streamwise impingement onto an axisymmetric obstacle is caused by a subcritical Hopf bifurcation, in contrast to supercritical Hopf bifurcation of the spiral vortex breakdown of [Gallaire et al. \(2006\)](#).

	Coefficients	$h = 0.5$	$h = 0.25$
Third order (WNL)	λ_1	$(6.10 + 5.14i) \times 10^1$	$(4.03 + 3.80i) \times 10^1$
	μ_1	$(2.94 - 7.30i) \times 10^{-1}$	$(1.25 - 2.91i) \times 10^{-1}$
Fifth order (DNS fit)	λ_2	$(2.04 + 5.77i) \times 10^5$	$(2.49 - 14.09i) \times 10^4$
	μ_2	$(10.86 - 0.94i) \times 10^2$	$(2.74 - 7.34i) \times 10^2$
	γ	$(-2.32 + 3.69i) \times 10^0$	$(-4.18 + 6.55i) \times 10^{-1}$

Table 2. Coefficients of the fifth-order Landau equations for $h = 0.5$ and $h = 0.25$. The third-order coefficients are computed by solving the WNL analysis. The fifth-order coefficients are fitted on the DNS data.

To fully characterize the nature of the Hopf bifurcation, we perform a WNL analysis. It provides, in addition, a powerful tool to obtain a model for this bifurcation with the resulting amplitude equation. Subcritical Hopf bifurcation requires to perform the expansion up to the fifth order. At the fifth order, the amplitude equation of a Hopf bifurcation is the Landau equation, which writes as

$$\frac{\partial a}{\partial t} - \epsilon^2(\lambda_1 + \epsilon^2\lambda_2)a - (\mu_1 + \epsilon^2\mu_2)a|a|^2 - \gamma a|a|^4 = 0, \tag{5.1}$$

with λ , μ and γ complex coefficients and a the complex amplitude. However, the radius of convergence regarding the bifurcation parameter decreases as we compute higher-order expansions. In both cases investigated, the WNL analysis fails to predict accurate coefficients at the fifth order, see figure 18 in appendix B. We, therefore, present the third-order coefficients which are combined with a numerical fit of the 3-D DNS to obtain the fifth-order coefficients, see table 2. This fit is based on the fluctuating kinematic energy.

Regarding the coefficients of the Landau equation, the μ_1 coefficients are always positive meaning that the quadratic nonlinearities destabilize the linear eigenmode in addition to the linear growth rate, represented by λ_1 . Only γ , the fifth-order term, stabilizes the amplitude equation. This is typical of a subcritical bifurcation. Such a bifurcation type is sensitive to external perturbation and the location of the vortex breakdown in experimental cases can be, therefore, very sensitive.

The amplitude equations are displayed in figure 9(a) and the corresponding frequencies are displayed in figure 9(b). The third-order solution of the WNL solution is represented by the dashed blue curves. The fluctuating kinematic energy of the 3-D DNS are displayed by the red dots, and the fifth-order amplitude equation is displayed by the red curves. The solid curves represent the stable branches and the dashed curves are unstable branches. As the Hopf bifurcation is subcritical, the third-order amplitude equation is unstable and the fifth-order amplitude equation stabilizes at an earlier Reynolds number than the critical Reynolds number. The frequency remains almost constant for the Reynolds number investigated.

The linear threshold characterized by the critical Reynolds number does not correspond to the only possible transition of the flow, the nonlinear threshold defining the hysteresis region appears for smaller Reynolds number and develops possibly first. The hysteresis range spans over $\Delta Re = 7$ for $h = 0.25$ and $\Delta Re = 10$ for $h = 0.5$. In both cases considered, the nonlinear thresholds appear for Reynolds larger than the turning point giving rise to the second, stable, branch in axisymmetric bifurcation diagram (see figure 5). Nevertheless, the 3-D solution shows only the spiral mode and no recirculation regions

Vortex impingement onto an axisymmetric obstacle

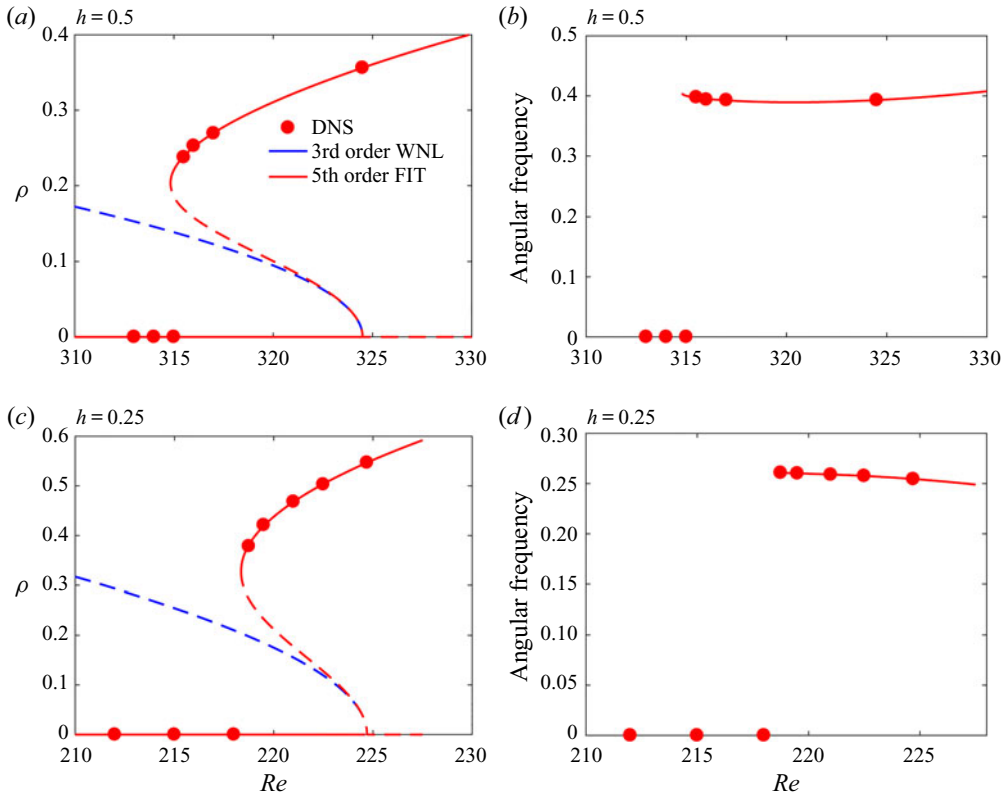


Figure 9. Limit cycle amplitude (a,c), and frequency (b,d) predicted by the third- and fifth-order amplitude equations for $S = 1.0$, $h = 0.5$ (a,b) and $h = 0.25$ (c,d), where $a = \rho e^{i\psi}$ as defined in (5.1).

are observed. Due to the nature of the bifurcation, which is very sensitive to disturbance, the eventuality to see the recirculation bubble for such a swirling flow, submitted to an adverse pressure gradient, is unlikely for the considered 3-D configurations.

6. Lateral displacement of the vortex

The vortex dynamics induced by a lateral displacement of the obstacle is summarized in the bifurcation diagram portrayed in figure 10. This bifurcation diagram is produced by displaying the successive minima and the maxima of a time series recorded at the location $(\tilde{R}, \tilde{\theta}, \tilde{Z}) = (0.5, 0.0, 18.0)$. Therefore, limit cycle solutions appear as two points, while more complex orbits such as quasi-periodic states or chaotic states display a dispersed distribution of points.

Figure 10 shows that the vortex dynamics preserves its periodicity below the lateral displacement $D < 0.1$. In this limit, which can be considered as small, the obstacle appears still as a flat wall for the vortex and does not disturb the sub-critical unstable mode of the vortex. The displacement required to fully stabilize the unstable spiralling mode is $D = 0.2$, where the vortex is seen to manage to escape the obstacle. A single point is displayed in figure 10, meaning that a steady-state solution is retrieved.

Complex orbits are observed in this bifurcation diagram for a lateral displacement between $D = 0.1$ and $D = 0.16$. These quasi-periodic or chaotic states exhibit the nonlinear interactions induced by the misalignment of the vortex centre and the obstacle.

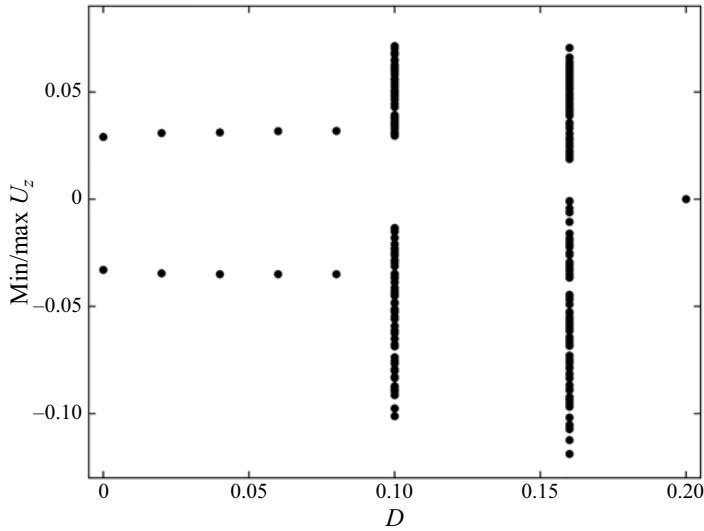


Figure 10. Bifurcation diagram of the min-max temporal series of the axial velocity of the 3-D DNS at $(\tilde{X}, \tilde{Y}, \tilde{Z}) = (0.5, 0.0, 18.0)$ as a function of the obstacle lateral displacements D at $S = 1.0$, $Re = 224.6$ and $h = 0.25$.

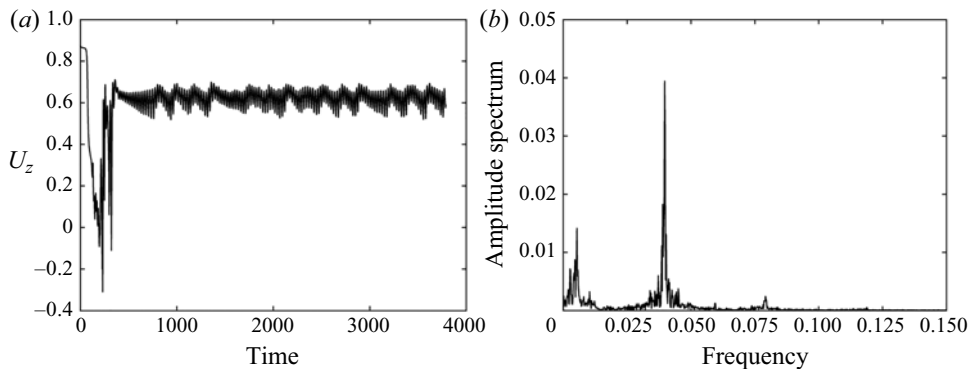


Figure 11. Time series (a) and amplitude Fourier spectrum (b) of the 3-D DNS at $(\tilde{X}, \tilde{Y}, \tilde{Z}) = (0.5, 0.0, 18.0)$ for $S = 1.0$, $Re = 224.6$, $h = 0.25$, and $D = 0.1$.

The associated time series and amplitude Fourier spectrum is displayed in [figure 11](#) for the representative case of $D = 0.1$. The transient phase, which ends at $t = 1600$, is removed from the Fourier analysis. The flow solution evolves toward a more complex orbit, where the main frequency of the spiralling motion is kept, and low-frequency modulations of the signal develop.

Visualizations of the flow solutions using the lambda 2 criterion are displayed in [figure 12](#). [Figure 12\(a\)](#) represents the flow solution for a lateral displacement of $D = 0.16$. The main spiral is observed, with smaller vortices inside the main recirculation region. In addition, the steady flow solution for lateral displacement of $D = 0.2$ is displayed in [figure 12\(b\)](#). A horseshoe vortex develops in front of the obstacle with a stronger branch where most of the vorticity is redirected as the vortex circumvents the obstacle.

An amplitude Fourier spectrum is displayed in [figure 13](#) for $D = 0.16$. The low-frequency oscillations are axisymmetric pulsations of the flow with residual

Vortex impingement onto an axisymmetric obstacle

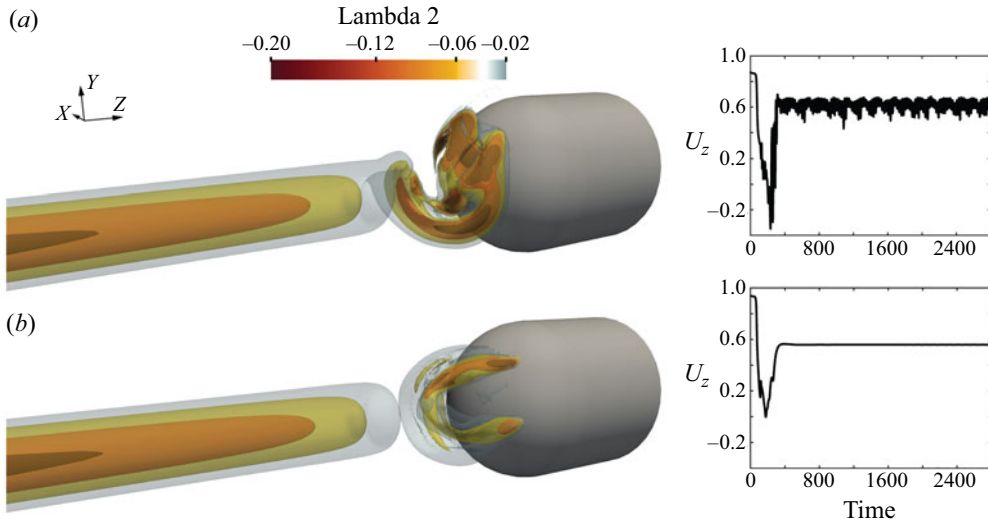


Figure 12. Λ_2 criterion of the 3-D DNS for $S = 1.0$, $Re = 224.6$, $h = 0.25$ and $D = 0.16$ (a), $D = 0.2$ (b), and their associated time series at the probe location $(\tilde{X}, \tilde{Y}, \tilde{Z}) = (0.5, 0.0, 18.0)$.

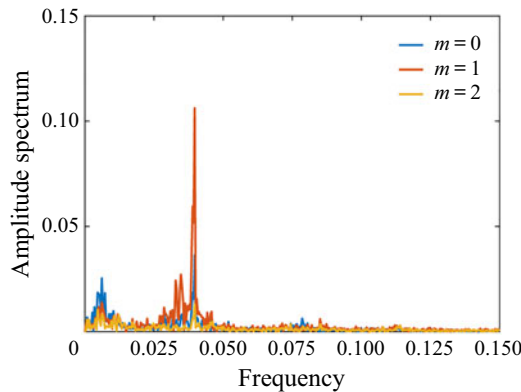


Figure 13. Amplitude Fourier spectrum decomposed in azimuthal wavenumber of the 3-D DNS at $(\tilde{X}, \tilde{Y}, \tilde{Z}) = (0.24, 0, 18.75)$ for azimuthal velocity and $S = 1.0$, $Re = 224.6$, $h = 0.25$ and $D = 0.16$.

oscillations of a double helix that can be associated with a flow structure developing in the recirculation zone between the obstacle and the spiralling vortex. It should be noticed that this double helix, which rotates at low frequency, is a mode reported in the modal analysis for the axisymmetric solution in figure 6(d). The main frequency peak is mainly composed of the single helix spiral and partially of the previously mentioned axisymmetric pulsation. Such a type of scenario is typically due to the quadratic nonlinearity of the Navier–Stokes equations. The lateral displacement of the obstacle can be associated with a steady mode of azimuthal wavenumber $m = 1$, which interacts with the main single spiral mode generating axisymmetric oscillations. This scenario has already been reported in Francis turbines with the generation of a synchronous pressure (Nishi *et al.* 1984; Pasche *et al.* 2019) and in the spiral vortex breakdown where several single helical modes generate axisymmetric pulsations (Pasche *et al.* 2018a).

7. Discussion and conclusion

We have investigated the dynamics of a vortex submitted to an adverse pressure gradient modelled by a Batchelor vortex impinging onto an axisymmetric obstacle. First, a parametric study of the vortex dynamics is performed: the Reynolds number, swirl number and obstacle radius are varied. Second, the obstacle is moved laterally to investigate the stabilization mechanism of the vortex, while it circumvents the obstacle.

The parametric study of the present swirling wake flow on the 2-D axisymmetric configuration shows the development of a bubble vortex breakdown, whose dynamics is associated with a saddle-node bifurcation. This bifurcation map of the bubble vortex breakdown has already been reported by Lopez (1994) and Meliga & Gallaire (2011) in a different configuration: a swirling jet flow induced by a contraction of the pipe radius. In the present study, on the first stable branch of the saddle-node bifurcation, a recirculation zone develops in front of the obstacle, which remains attached to the obstacle. On the second stable branch, a recirculation bubble develops that is identified as a vortex breakdown bubble. At larger swirl and Reynolds numbers, the adverse pressure gradient pushes the bubble against the inlet of the computational domain, while for an intermediate swirl and Reynolds number, the bubble vortex breakdown moves progressively upstream. Finally, below a swirl threshold, the saddle-node bifurcation vanishes.

The intensity of the adverse pressure gradient induces a shift of the bifurcation to lower Reynolds and swirl numbers. This characteristic has already been observed for adverse pressure gradients induced by an air intake (Delery 1994) and in a vortex impinging a sphere (Pasche *et al.* 2014). In addition, at larger Reynolds numbers, multiple saddle-node bifurcations are identified for the larger obstacle radius investigated. This behaviour, only valid for 2-D axisymmetric configuration, is connected to the second recirculation region that develops in the wake of the bubble vortex breakdown and is attached to the obstacle. The reversal swirling flow allows the onset of a second vortex breakdown phenomenon having a similar configuration as the closed container experiments (Escudier 1984).

Not only saddle-node bifurcations are tracked, but also the Hopf bifurcations. These bifurcations correspond to the development of a marginally unstable mode of azimuthal wavenumber $m = 1$, corresponding to a single helical spiral. In the present configuration, the Hopf transition appears at a smaller Reynolds number than the first saddle-node transition. This scenario is confirmed by 3-D DNS, which shows a single helical vortex breakdown. Moreover, this single helical spiral develops in the absence of a recirculation bubble. The mechanism for the generation of this single helical mode is identical to the one identified by Gallaire *et al.* (2006). This spiral mode results from a hydrodynamic instability growing due to the swirling wake flow profile. However, the spiral forming in the wake of a recirculation bubble is due to a supercritical Hopf bifurcation, while in the present case, we identify a sub-critical Hopf bifurcation through a WNL analysis. We perform this analysis up to the fifth order to describe the saturation amplitude. The consequences are that the transition is very sensitive to small disturbances present, for instance, in the boundary layer. A hysteresis region appears where two different thresholds can be defined: the linear threshold associated with the marginally unstable linear mode and the nonlinear threshold associated with a smaller Reynolds number. The nonlinear threshold associated with the backward Hopf bifurcation appears for a Reynolds number larger than the fold point giving birth to the second stable branch of the axisymmetric saddle-node bifurcation. However, we never observe a recirculation bubble in the 3-D DNS, and the development of the spiral vortex breakdown is not accompanied a recirculation bubble. It should be mentioned that the 2-D axisymmetric solution at the turning point giving birth to the second stable saddle-node branch does not display a recirculation bubble which is consistent with the 3-D DNS. The recirculation bubble is

formed later on this branch. Thus, swirling jet flow impinging a downstream obstacle leads to a spiral vortex breakdown induced by a sub-critical Hopf bifurcation bypassing the classical bubble vortex breakdown.

Swirling wake flows can stand axisymmetric waves as demonstrated by Benjamin (1962) and Mager (1972). Two-dimensional axisymmetric direct numerical simulations of swirling wake flows in an unconfined domain, performed by Ruith *et al.* (2003), stress that these standing waves lead to the bubble vortex breakdown. In the present case, the axisymmetric solutions do not recover such a recirculation region. The main difference is that the present vortex is free of inlet disturbance while in the case of Ruith *et al.* (2003), the recirculation bubble hits the inlet boundary. Therefore, swirling wake flow could become first unstable to the helical mode instead of axisymmetric standing waves. Minimal energy principle can be stressed where forming a single helical spiral is more efficient than forming an axisymmetric recirculation bubble with helical unstable wake flow.

The second part of the present study is focused on the stabilization mechanism of this spiral vortex breakdown caused by an off-centre displacement of the downstream axisymmetric obstacle for the smaller aspect ratio (half of the vortex core size divided by the obstacle radius). A small lateral displacement of the obstacle does not disturb the amplitude of the spiral and does not significantly affect its frequency. For a larger displacement, the vortex reaches a quasiperiodic state or chaotic state characterized by the onset of non-commensurable frequencies with the main frequency of the single helical mode. We observe in the 3-D DNS the formation of a second mode growing inside the recirculation region of the spiral. This mode has been predicted by the global stability analysis on the 2-D axisymmetric configuration as a double helical spiral ($m = 2$) rotating at a lower frequency than the main spiral. We also see the formation of an axisymmetric oscillation of the flow as observed when multiple single helical modes exist. The displacement of the obstacle can be modelled as a stationary $m = 1$ mode that by nonlinear interactions produces an axisymmetric pulsation of the flow. This mechanism has been reported for the spiral vortex breakdown (Pasche *et al.* 2018a) and hydraulic turbines (Pasche *et al.* 2019) as a plunging wave. The quasiperiodic or chaotic state persists for increasing lateral displacements up to the point where the vortex stabilizes as a horseshoe vortex with a strong and weak secondary vortex circumventing the obstacle. We did not succeed in capturing this dynamics by a WNL analysis including a domain perturbation method to predict the lateral displacement required to stabilize the vortex. In the present case, the obstacle radius could already be too large to be in the validity range of the fifth-order WNL analysis.

Helical vortex breakdown without a recirculation bubble has been observed by Billant *et al.* (1998) when a swirling jet flow enters in an unbounded container. Billant *et al.* (1998) characterized the helical mode as a prebreakdown state because the recirculation bubble appears at a larger swirl number. The observed helical mode has two branches growing radially as they propagate. Radial velocity contribution to spiral vortex breakdown is also observed in the work of Meliga *et al.* (2012) where a pipe contraction is used to favour vortex breakdown. At low swirl number, a self-sustained instability of single helical mode appears before the formation of the bubble (see figure 4 in this reference). In addition, Mattner *et al.* (2002) show experimentally using a vortex generator that the development of a spiralling vortex as a transient structure on the top of a bubble vortex breakdown, when a sudden radial disturbance is applied by modifying the guide vane angle. Based on the present study and these examples, we argue that the non-parallel character of the vortex inducing a radial velocity component contributes to the distinction of the spiral vortex breakdown with and without a recirculation bubble. Moreover, unsteady flow simulations

of hydraulic Francis turbines operating at part load conditions show the development of a single helical mode without a recirculation bubble as a consequence of the radial velocity contribution at the inlet of the draft tube (Pasche, Avellan & Gallaire 2017) while a steady recirculation bubble is observed for the solution based on the axisymmetric Reynolds averaged Navier–Stokes equations (see Susan-Resiga *et al.* 2006). In a swirl burner, similar behaviour has been observed by Jochmann *et al.* (2006). In the study of Tammisola & Juniper (2016) and Oberleithner *et al.* (2011), the contribution of the radial velocity is more ambiguous because the recirculation bubble reaches the nozzle, forcing the development of the single helical mode to be radial. It is already well known that helical disturbances can be triggered by parallel swirling flow as demonstrated by Delbende, Chomaz & Huerre (1998) with the convective/absolute instability analysis of one-dimensional Batchelor vortex profile or by Heaton, Nichols & Schmid (2009) for the 2-D counterpart. However, the presence of a radial velocity could also trigger a helical instability of a single helical mode. The local temporal stability analysis of a non-parallel vortex has been investigated by Fernandez-Feria (1996). Self-similar one-dimensional vortex profiles matching the viscous core and the potential region define a family of base flows, which are dependent on the axial coordinate inducing a non-zero radial velocity component. The temporal stability analysis of these vortex profiles shows that these vortex profiles are unstable for non-axisymmetric disturbances. Thus, further investigations are required to distinguish the contribution of the radial velocity to the vortex breakdown dynamics.

Ultimately, we observe that, in the present investigation, the adverse pressure gradient tends to make vortices unstable to helical disturbances at lower swirl numbers than classical spiral vortex breakdown induced by a recirculation bubble. Such a type of spiral vortex breakdown without a recirculation region has already been observed by Lambourne & Bryer (1962) and Delery (1994) and we show that it develops here as a subcritical Hopf bifurcation.

Declaration of interests. The authors report no conflict of interest.

Author ORCID.

 S. Pasche <https://orcid.org/0000-0003-0229-8878>.

Appendix A. Direct numerical flow simulation validation

A.1. Two-dimensional axisymmetric solver

All the computations are carried out by means of the finite element library Freefem++ (Hecht 2012) in a 2-D axisymmetric domain. The steady axisymmetric incompressible Navier–Stokes equations are first premultiplied by R to avoid the axis singularity and then solved numerically via a Newton–Raphson iterative method. We use the unsymmetric multifrontal sparse lower-upper factorization package (UMFPACK) to solve steady Navier–Stokes equations. The computational domain is meshed by approximately 260 000 triangular Taylor–Hood elements, $P_2 - P_1$ polynomial-order elements for the velocity–pressure unknowns. The tolerance to obtaining a converged solution is defined as 10^{-8} using the H_1 -norm. The arc-length continuation method uses the same specification. The initial increment on the Reynolds number is 15, which can be adapted if the radius of convergence of the method becomes smaller. The tracking algorithms require more computational resources as the system to solve is extended with eigenvectors of the linearized Navier–Stokes equations. Therefore the tolerance for convergence is relaxed

Vortex impingement onto an axisymmetric obstacle

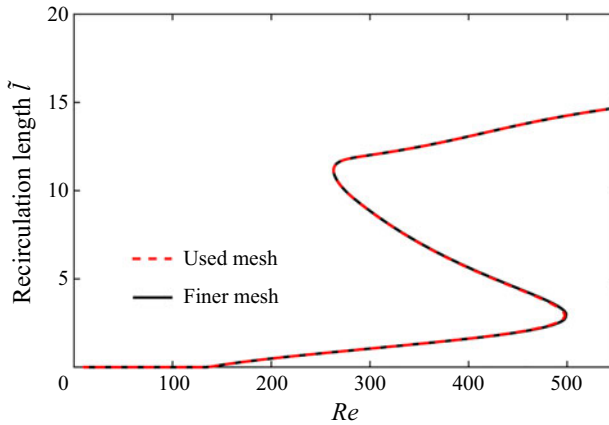


Figure 14. Validation of the 2-D axisymmetric continuation method for $S = 1.0$, $h = 0.5$.

to 10^{-5} on the residual L_2 norm of the incremental errors on the bifurcation parameter. It should be also noticed that both tracking algorithms are solved in the complex variable. The eigenvalue problem is solved by the implicit restarted Arnoldi method of the ARPACK library embedded in the FreeFem++ library. The eigenvalues are obtained with a tolerance of 10^{-6} of the ARPACK solver.

The continuation method has been validated using a finer mesh of approximately 420 000 triangular Taylor–Hood elements. The convergence results are portrayed in figure 14.

A.2. Three-dimensional solver

Direct numerical flow simulations are performed using NEK5000. The mesh used for the computation is presented in figure 15. It is refined close to the vortex core and before the obstacle nose, while it is stretched approaching the lateral boundaries. The mesh is created using ICEM CFX to properly define an O-grid topology that matches the spherical nose of the obstacle and minimizes skewed cells. Eighty per cent of the cells have a minimum angle larger than 80 degrees. Only a few cells, 0.09 %, have minimum angles between 25 and 45 degrees. No convergence issues are induced by these cells. The mesh is then transferred to NEK5000 in its native format using Matlab software. The computational domain is bounded by the Batchelor vortex equation (2.1) on the inlet boundary Γ_{in} , a free-outflow condition $(-PI + Re^{-1} \cdot (\nabla V)) \cdot \mathbf{n} = 0$ on the external boundary Γ_{ext} , a convective condition $\partial_t V + U_c \cdot \partial_n V = 0$ on the outlet boundary Γ_{out} and a no-slip condition on the obstacle Γ_{obs} . We have fixed the convective velocity to be equal to the free-stream velocity $U_c = (0, 0, 1)$. The solution obtained is checked using a second computation where the polynomial order is increased. The temporal discretization of the nonlinear terms is treated explicitly by a third-order backward-differentiation scheme combined with a third-order extrapolation scheme. The linear terms are treated implicitly in time and a pressure–velocity decoupling method is used for the spatial discretization. The velocity and pressure space are represented by a tensor-product array of Gauss–Lobatto–Legendre and Gauss–Legendre points of polynomial orders N and $N - 2$. In the present study, a $P_8 - P_6$ polynomial order for velocity–pressure with 92 652 hexahedral elements is required to compute the flow field.

The mesh is not modified to perform the convergence analysis, only the polynomial order of the element is increased. The parameters for this analysis are displayed in table 3.

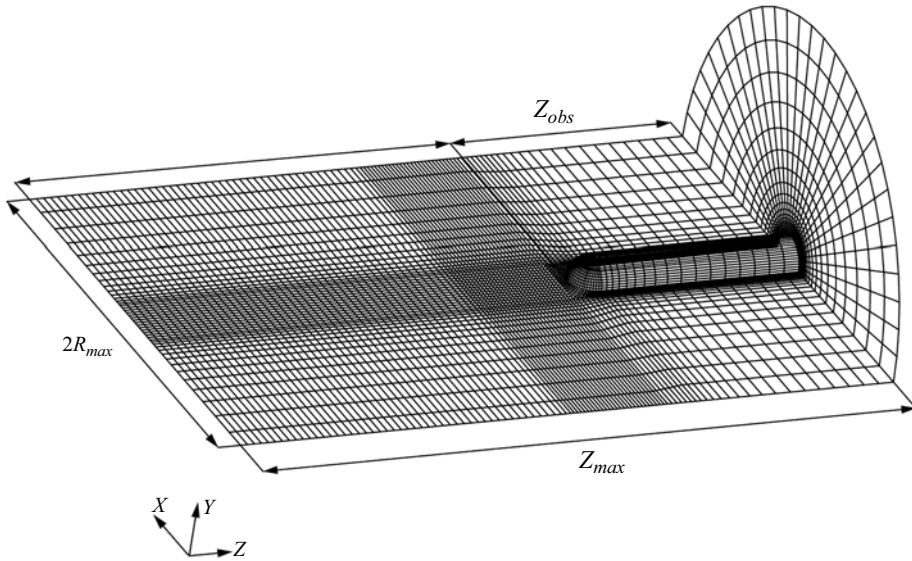


Figure 15. Half of the mesh defining the spectral elements of the 3-D computational domain.

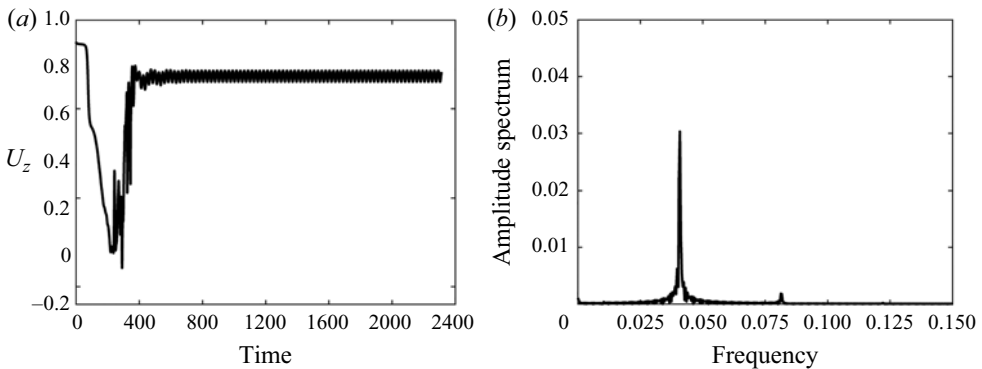


Figure 16. Time series (a) and amplitude Fourier spectrum (b) at the monitoring point $(\tilde{X}, \tilde{Y}, \tilde{Z}) = (0.5, 0.0, 18.0)$ for the axial velocity of the 3-D finer DNS at $S = 1.0$, $Re = 224.6$ and $h = 0.25$.

Case	Boundary condition on Γ_{ext}	nb elements	Discretization	Courant-Friedrichs-Lewy number	h	3-D (Amp, freq)
M1	Freestress	92 652	$P_8 - P_6$	0.3	0.25	(0.0289, 0.0408)
M2	Freestress	92 652	$P_{10} - P_8$	0.3	0.25	(0.0303, 0.0408)

Table 3. Convergence of the 3-D numerical flow simulations.

The time series and the amplitude Fourier spectrum at the monitoring point for the finer discretization are displayed in figure 16. A limit cycle solution is obtained for the bifurcation parameters $S = 1.0$ and $Re = 224.6$ as for the coarser discretization. In table 3, the frequency and the amplitude of the signal for the two discretizations are reported, and a good agreement is obtained. Thus, we consider that the used discretization is sufficiently small to capture the nonlinear dynamics of the vortex impinging an obstacle.

Azimuthal wavenumber	Boundary conditions
$m = 0$	$u_R = u_\theta = 0, \partial_R u_Z = 0$
$m = \pm 1$	$u_Z = p = 0, \partial_R u_R = \partial_R u_\theta = 0$
$m > 1$	$u_R = u_\theta = u_Z = 0$

Table 4. Boundary conditions on the axisymmetric axis applied to the disturbances for different azimuthal wavenumbers.

Appendix B. Weakly nonlinear analysis fifth order

The derivation of the equations for the WNL analysis follows the derivation of Fujimura (1991). We first recall the asymptotic expansion regarding the parameter ϵ with the slow time scale acting at ϵ^2 :

$$\mathbf{q} = \mathbf{q}_0 + \epsilon \mathbf{q}_1 + \epsilon^2 \mathbf{q}_2 + \epsilon^3 \mathbf{q}_3 + \epsilon^4 \mathbf{q}_4 + \epsilon^5 \mathbf{q}_5 + \text{h.o.t.} \tag{B1}$$

Inserting this expansion in the Navier–Stokes equations and collecting the terms at different orders yields the following systems of equations to be solved. It should be noticed that the boundary conditions applied to the axisymmetric configuration are the Batchelor vortex at the inlet, free outflow on the external and outlet boundary, no slip on the obstacle and the axis and the boundary is dependent of the azimuthal wavenumber, see table 4.

At order ϵ^0 , the base flow solution \mathbf{q}_0 of the axisymmetric governing equations is retrieved

$$\mathcal{M}\mathbf{q}_0 + \mathcal{N}(\mathbf{q}_0, \mathbf{q}_0) = \mathbf{0}, \tag{B2}$$

where \mathcal{M} regroups the pressure gradient, divergence and the diffusive term and \mathcal{N} the nonlinear convective term (see figure 17).

At order ϵ^1 , the linearized Navier–Stokes equations are obtained. Since we deal with an axisymmetric formulation of the governing equation, an azimuthal Fourier series decomposition is applied and each azimuthal wavenumber $m \in \mathcal{Z}$ is investigated to recover the full spectrum of the flow. However, at this order, the only growing mode is associated with the first azimuthal wave. The solution reads

$$\mathbf{q}_1 = A_1(T_2, T_4) \mathbf{q}_{1A_1} \exp(i\theta - i\omega t) + A_1^*(T_2, T_4) \mathbf{q}_{1A_1}^* \exp(-i\theta + i\omega t), \tag{B3}$$

with $A_1(T_2, T_4)$ the amplitude of the general solution which is a function of the slow times only (see figure 17). This amplitude is unknown at that stage and will be the result of this WNL analysis. In this relation, the symbol $*$ defined the complex conjugate. The eigenvalue system associated with this solution writes

$$((\omega_i - i\omega_r)\mathcal{B} + \mathcal{L}_m(\mathbf{q}_0))\mathbf{q}_{1A_1} = \mathbf{0}, \tag{B4}$$

with \mathcal{B} the temporal operator and the spatial operator gathering the linearized convective operator, the diffusive operator, the pressure gradient and the incompressibility condition

$$\mathcal{L}_m(\mathbf{q}_0)\mathbf{q} = \left(\begin{array}{c} \nabla \mathbf{u} \cdot \mathbf{u}_0 + \nabla \mathbf{u}_0 \cdot \mathbf{u} - \frac{1}{Re_c} \nabla_m^2 \mathbf{u} + \nabla p \\ \nabla \cdot \mathbf{u} \end{array} \right). \tag{B5}$$

The following normalization of the eigenmode is considered:

$$\langle \mathbf{u}_{1A_1}, \mathbf{u}_{1A_1}^* \rangle = \int_S \mathbf{u}_{1A_1} \cdot \mathbf{u}_{1A_1}^* R dR dZ = 1, \tag{B6}$$

which makes the amplitude equation equal to the amplitude of the DNS disturbance.

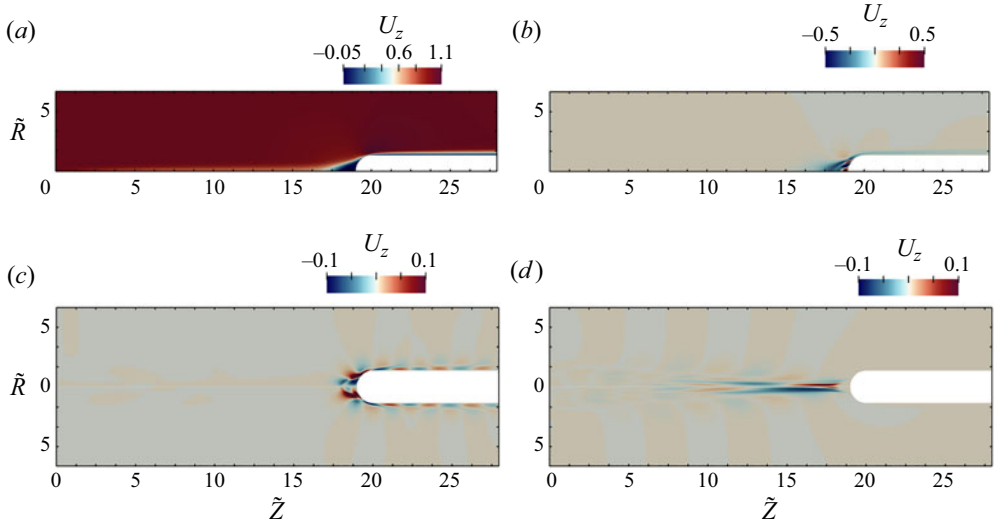


Figure 17. Base flow (a), mean flow correction (b), direct eigenmode (c) and adjoint eigenmode (d) at $Re = 224.6$, $S = 1.0$ and $h = 0.25$.

We anticipate the closure of the expansion that results in a non-resonant solution using the orthogonality condition. The adjoint eigenvector has to be orthogonal to the higher-order solution defining the first unstable eigenmode as the leading-order contribution. The normalization allows the system to satisfy the Fredholm alternative that defines uniquely the solution of the system

$$((\omega_i + i\omega_r)\mathcal{B} + \mathcal{L}_m^\dagger(q_0))q_{1A_1}^\dagger = \mathbf{0}, \tag{B7}$$

$$\langle \mathbf{u}_{1A_1}, \mathbf{u}_{1A_1}^\dagger \rangle = \int_S \mathbf{u}_{1A_1} \cdot \mathbf{u}_{1A_1}^\dagger R \, dR \, dZ = 1. \tag{B8}$$

At order ϵ^2 , the interaction between the two previous modes appears, generating three sets of equations spread by the azimuthal wavenumber m and temporal harmonics k of the initial modes coming from the general equations

$$\left(\frac{\partial \mathbf{u}_2}{\partial T_0} + \frac{\partial \mathbf{u}_0}{\partial T_2} + \mathcal{L}_m(q_0) \right) \mathbf{q}_2 = \mathbf{F}_2. \tag{B9}$$

The forcing term writes

$$\mathbf{F}_2 = \begin{pmatrix} -\delta \nabla_0^2 \mathbf{u}_0 \\ -|A_1|^2 2 \operatorname{Re}(\nabla_1 \mathbf{u}_{1A_1} \cdot \mathbf{u}_{1A_1}^*) \\ -A_1^2 \nabla_1 \mathbf{u}_{1A_1} \cdot \mathbf{u}_{1A_1} \exp(2i\theta - 2i\omega_c t) + \text{c.c.} \end{pmatrix}, \tag{B10}$$

with ω_c the angular frequency of the marginally unstable mode at the critical Reynolds number Re_c . In this equation, the base flow solution is time independent. It results trivially in zero for

$$\frac{\partial \mathbf{u}_0}{\partial T_2} = 0, \tag{B11}$$

while $\partial \mathbf{u}_2 / \partial T_0 = ik\omega_c \mathcal{B}$ after normal mode expansion, with $k \in \mathbb{Z}$. The linear properties of this equation imply the superposition principle. Therefore, each system is solved

independently to obtain the solution for each m and k , which strictly depends on the forcing amplitude

$$\mathbf{q}_2 = \mathbf{q}_{2\delta} + |A_1|^2 \mathbf{q}_{2|A_1|^2} + \left(A_1^2 \mathbf{q}_{2A_1^2} \exp(2i\theta - 2i\omega_c t) + \text{c.c.} \right). \quad (\text{B12})$$

A similar approach will be used for all system at the next orders.

At order ϵ^3 , distinguishing the different terms of the expansion yield the following equations:

$$\left(\frac{\partial \mathbf{u}_3}{\partial T_0} + \frac{\partial \mathbf{u}_1}{\partial T_2} + \mathcal{L}_m(\mathbf{q}_0) \right) \mathbf{q}_3 = \mathbf{F}_3, \quad (\text{B13})$$

where the forcing term writes

$$\mathbf{F}_3 = \begin{pmatrix} -A_1 \left[\nabla_1^2 \mathbf{u}_{1A_1} + \nabla_1 \mathbf{u}_{1A_1} \cdot \mathbf{u}_{2\delta} + \nabla_0 \mathbf{u}_{2\delta} \cdot \mathbf{u}_{1A_1} \right] \exp(i\theta - i\omega_c t) + \text{c.c.} \\ -A_1 |A_1|^2 \left[\nabla_1 \mathbf{u}_{1A_1} \cdot \mathbf{u}_{2|A_1|^2} + \nabla_0 \mathbf{u}_{2|A_1|^2} \cdot \mathbf{u}_{1A_1} \right. \\ \left. + \nabla_2 \mathbf{u}_{2A_1^2} \cdot \mathbf{u}_{1A_1}^* + \nabla_1 \mathbf{u}_{1A_1}^* \cdot \mathbf{u}_{2A_1^2} \right] \exp(i\theta - i\omega_c t) + \text{c.c.} \\ -A_1^3 \left[\nabla_1 \mathbf{u}_{1A_1} \cdot \mathbf{u}_{2A_1^2} + \nabla_2 \mathbf{u}_{2A_1^2} \cdot \mathbf{u}_{1A_1} \right] \exp(3i\theta - 3i\omega_c t) + \text{c.c.} \end{pmatrix}. \quad (\text{B14})$$

Using the superposition principle, three systems of equations have to be solved for A_1 , $A_1 |A_1|^2$ and A_1^3 . The last system presents no difficulties as it is a non-degenerate operator as for the previous orders. In contrast, the systems for A_1 , $A_1 |A_1|^2$ are degenerate. The solutions resonate with the forcing term. Thus this system is solved by extending the system with an inner product of the solution which has to be zero to avoid contribution to the kernel of the operator

$$\begin{pmatrix} -i\omega_c \mathcal{B} + \mathcal{L}_m(\mathbf{q}_0) & -\mathbf{u}_{1A_1} \\ \mathbf{u}_{1A_1}^\dagger & 0 \end{pmatrix} \begin{pmatrix} \mathbf{u}_{3\delta A_1} \\ \lambda \end{pmatrix} = \begin{pmatrix} \mathbf{F}_{3\delta} \\ 0 \end{pmatrix}. \quad (\text{B15})$$

The orthogonality condition is then strictly imposed using the relation

$$\mathbf{u}_{3\delta A_1} = \mathbf{u}_{3\delta A_1} - \frac{\langle \mathbf{u}_{3\delta A_1}, \mathbf{u}_{1A_1}^\dagger \rangle}{\langle \mathbf{u}_{1A_1}, \mathbf{u}_{1A_1}^\dagger \rangle} \mathbf{u}_1, \quad (\text{B16})$$

satisfying exactly

$$\langle \mathbf{u}_{3\delta A_1}, \mathbf{u}_{1A_1}^\dagger \rangle = 0. \quad (\text{B17})$$

The same technique is used for the second degenerate solution, leading to the second normalization

$$\langle \mathbf{u}_{3A_1 |A_1|^2}, \mathbf{u}_{1A_1}^\dagger \rangle = 0. \quad (\text{B18})$$

At this order, this compatibility condition has to be solved using the Fredholm alternative. It results in the third-order amplitude equation given by

$$\frac{\partial A_1}{\partial T_2} + \lambda_1 A_1 + \mu_1 A_1 |A_1|^2 = 0, \quad (\text{B19})$$

$S = 1.0, Re = 164$	λ_1	μ_1	μ_{1i}/μ_{1r}
Present	$30.1 + 22.4i$	$0.531 - 1.61i$	3.03
Meliga <i>et al.</i> (2012)	$28.1 + 21.8i$	$0.545 - 1.63i$	2.99

Table 5. Validation of the WNL analysis up to the third order for the vortex breakdown induced by a Grabowsky vortex.

	Coefficients	$h = 0.5$	$h = 0.25$
Third order (WNL)	λ_1	$(6.1 + 5.14i) \times 10^1$	$(4.03 + 3.80i) \times 10^1$
	μ_1	$(2.94 - 7.30i) \times 10^{-1}$	$(1.25 - 2.91i) \times 10^{-1}$
Fifth order (WNL)	λ_2	$(11.28 + 2.38i) \times 10^4$	$(8.43 + 2.88i) \times 10^4$
	μ_2	$(-2.22 + 1.77i) \times 10^3$	$(-8.49 + 9.30i) \times 10^2$
	γ	$(-1.35 + 1.34i) \times 10^1$	$(-3.40 + 4.66i) \times 10^0$
Fifth order (DNS fit)	λ_2	$(2.04 + 5.77i) \times 10^5$	$(2.49 - 14.09i) \times 10^4$
	μ_2	$(10.86 - 0.94i) \times 10^2$	$(2.74 - 7.34i) \times 10^2$
	γ	$(-2.32 + 3.69i) \times 10^0$	$(-4.18 + 6.55i) \times 10^{-1}$

Table 6. Coefficients of the fifth-order Landau equations for $h = 0.5$ and $h = 0.25$. The third- and fifth-order coefficients are computed by solving the WNL analysis.

where the coefficients express as

$$\lambda_1 = \langle \nabla_1 \mathbf{u}_{1A_1} \cdot \mathbf{u}_{2\delta} + \nabla_0 \mathbf{u}_{2\delta} \cdot \mathbf{u}_{1A_1} + \delta_\nu \nabla_1^2 \mathbf{u}_{1A_1}, \mathbf{u}_{1A_1}^\dagger \rangle, \tag{B20}$$

$$\mu_1 = \langle \nabla_1 \mathbf{u}_{1A_1} \cdot \mathbf{u}_{2|A_1|^2} + \nabla \mathbf{u}_{2|A_1|^2} \cdot \mathbf{u}_{1A_1} + \nabla_1 \mathbf{u}_{1A_1}^* \cdot \mathbf{u}_{2A_1^2} + \nabla_2 \mathbf{u}_{2A_1^2} \cdot \mathbf{u}_{1A_1}^*, \mathbf{u}_{1A_1}^\dagger \rangle. \tag{B21}$$

The coefficient λ_1 is associated with the growth rate of the nonlinear amplitude and μ_1 represents the nonlinear damping of the quadratic term.

The solution at this order writes

$$\mathbf{q}_3 = \left(\left[A_1 \mathbf{q}_{3\delta} + A_1 |A_1|^2 \mathbf{q}_{3A_1|A_1|^2} + A_2 \mathbf{q}_{1A_1} \right] \exp(i\theta - i\omega_c t) + \text{c.c.} \right) \tag{B22}$$

$$+ \left(A_1^3 \mathbf{q}_{3A_1^3} \exp(3i\theta - 3i\omega_c t) + \text{c.c.} \right). \tag{B23}$$

The validation of the third-order term is performed by reproducing the WNL analysis of the vortex breakdown configuration of Meliga *et al.* (2012): a supercritical Hopf bifurcation. The ratio between the imaginary part and the real part of the saturation coefficients has to be constant for any normalization of the analysis as demonstrated by Dusek *et al.* (1994), see table 5. We report the results of the WNL analysis up to the fifth order in table 6.

At order ϵ^4 , a second amplitude A_2 is introduced having the same unstable mode as A_1 .

$$\left(\frac{\partial \mathbf{u}_4}{\partial T_0} + \frac{\partial \mathbf{u}_2}{\partial T_2} + \mathcal{L}_m(\mathbf{q}_0) \right) \mathbf{q}_4 = \mathbf{F}_4, \tag{B24}$$

where the forcing term writes

$$\mathbf{F}_4 = \left(\begin{array}{l} -A_1^2 \left[\nabla_1^2 \mathbf{u}_{2A_1^2} + \nabla_1 \mathbf{u}_{1A_1} \cdot \mathbf{u}_{3\delta A_1} + \nabla_1 \mathbf{u}_{3\delta A_1} \cdot \mathbf{u}_{1A_1} \right. \\ \left. + \nabla_0 \mathbf{u}_{2\delta} \cdot \mathbf{u}_{2A_1^2} + \nabla_2 \mathbf{u}_{2A_1^2} \cdot \mathbf{u}_{2\delta} \right] \exp(2i\theta - 2i\omega_c t) + \text{c.c.} \\ -|A_1|^2 \left[\nabla_1^2 \mathbf{u}_{2|A_1|^2} + 2\text{Re} \left(\nabla_1 \mathbf{u}_{3\delta A_1} \cdot \mathbf{u}_{1A_1}^* \right) + 2\text{Re} \left(\nabla_1 \mathbf{u}_{1A_1} \cdot \mathbf{u}_{3\delta A_1}^* \right) \right. \\ \left. + \nabla_0 \mathbf{u}_{2\delta} \cdot \mathbf{u}_{2|A_1|^2} + \nabla_0 \mathbf{u}_{2|A_1|^2} \cdot \mathbf{u}_{2\delta} \right] \\ -A_1^2 |A_1|^2 \left[\nabla_1 \mathbf{u}_{1A_1} \cdot \mathbf{u}_{3A_1|A_1|^2} + \nabla_1 \mathbf{u}_{3A_1|A_1|^2} \cdot \mathbf{u}_{1A_1} + \nabla_1 \mathbf{u}_{1A_1}^* \cdot \mathbf{u}_{3A_1^3} \right. \\ \left. + \nabla_3 \mathbf{u}_{3A_1^3} \cdot \mathbf{u}_{1A_1}^* + \nabla_2 \mathbf{u}_{2A_1^2} \cdot \mathbf{u}_{2|A_1|^2} + \nabla_0 \mathbf{u}_{2|A_1|^2} \cdot \mathbf{u}_{2A_1^2} \right] \exp(2i\theta - 2i\omega_c t) + \text{c.c.} \\ -|A_1|^4 \left[2\text{Re} \left(\nabla_1 \mathbf{u}_{3A_1|A_1|^2} \cdot \mathbf{u}_{1A_1}^* \right) + 2\text{Re} \left(\nabla_1 \mathbf{u}_{1A_1} \cdot \mathbf{u}_{3A_1|A_1|^2}^* \right) \right. \\ \left. + \nabla_0 \mathbf{u}_{2|A_1|^2} \cdot \mathbf{u}_{2|A_1|^2} \right] \\ -A_1^4 \left[\nabla_1 \mathbf{u}_{1A_1} \cdot \mathbf{u}_{3A_1^3} + \nabla_3 \mathbf{u}_{3A_1^3} \cdot \mathbf{u}_{1A_1} + \nabla_2 \mathbf{u}_{2A_1^2} \cdot \mathbf{u}_{2A_1^2} \right] \exp(4i\theta - 4i\omega_c t) + \text{c.c.} \\ -A_1 A_2 \left[2\text{Re} \left(\nabla_1 \mathbf{u}_{1A_1} \cdot \mathbf{u}_{1A_1} \right) \right] \exp(2i\theta - 2i\omega_c t) + \text{c.c.} \\ -A_1^* A_2 \left[2\text{Re} \left(\nabla_1 \mathbf{u}_{1A_1} \cdot \mathbf{u}_{1A_1}^* \right) \right] \end{array} \right). \tag{B25}$$

The full development of $\partial \mathbf{u}_2 / \partial T_2$ must be included in this equation, which writes

$$\frac{\partial \mathbf{u}_2}{\partial T_2} = - \left[(\lambda + \lambda^*) |A_1|^2 + (\mu + \mu^*) |A_1|^4 \right] \mathbf{u}_{2|A_1|^2} \tag{B26}$$

$$- \left[2\lambda A_1^2 + 2\mu A_1^2 |A_1|^2 \right] \mathbf{u}_{2A_1^2} \tag{B27}$$

$$- \left[2\lambda^* A_1^{2*} + 2\mu^* A_1^{2*} |A_1|^2 \right] \mathbf{u}_{2A_1^{2*}}. \tag{B28}$$

The solution at this order is given by

$$\mathbf{q}_4 = |A_1|^2 \mathbf{q}_{4|A_1|^2} + A_1^* A_2 \mathbf{q}_{4|A_1|^2} + |A_1|^4 \mathbf{q}_{4|A_1|^4} \tag{B29}$$

$$+ \left(\left[A_1^2 \mathbf{q}_{4A_1^2} + A_1 A_2 \mathbf{q}_{4A_1^2} + A_1^2 |A_1|^2 \mathbf{q}_{A_1^2|A_1|^2} \right] \exp(2i\theta - 2i\omega_c t) + \text{c.c.} \right) \tag{B30}$$

$$+ \left(\left[A_1^4 \mathbf{q}_{4A_1^4} \right] \exp(4i\theta - 4i\omega_c t) + \text{c.c.} \right). \tag{B31}$$

At order ϵ^5 , the following system is obtained:

$$\left(\frac{\partial \mathbf{u}_5}{\partial T_0} + \frac{\partial \mathbf{u}_3}{\partial T_2} + \frac{\partial \mathbf{u}_1}{\partial T_4} + \mathcal{L}_m(\mathbf{q}_0) \right) \mathbf{q}_5 = \mathbf{F}_5, \tag{B32}$$

Vortex impingement onto an axisymmetric obstacle

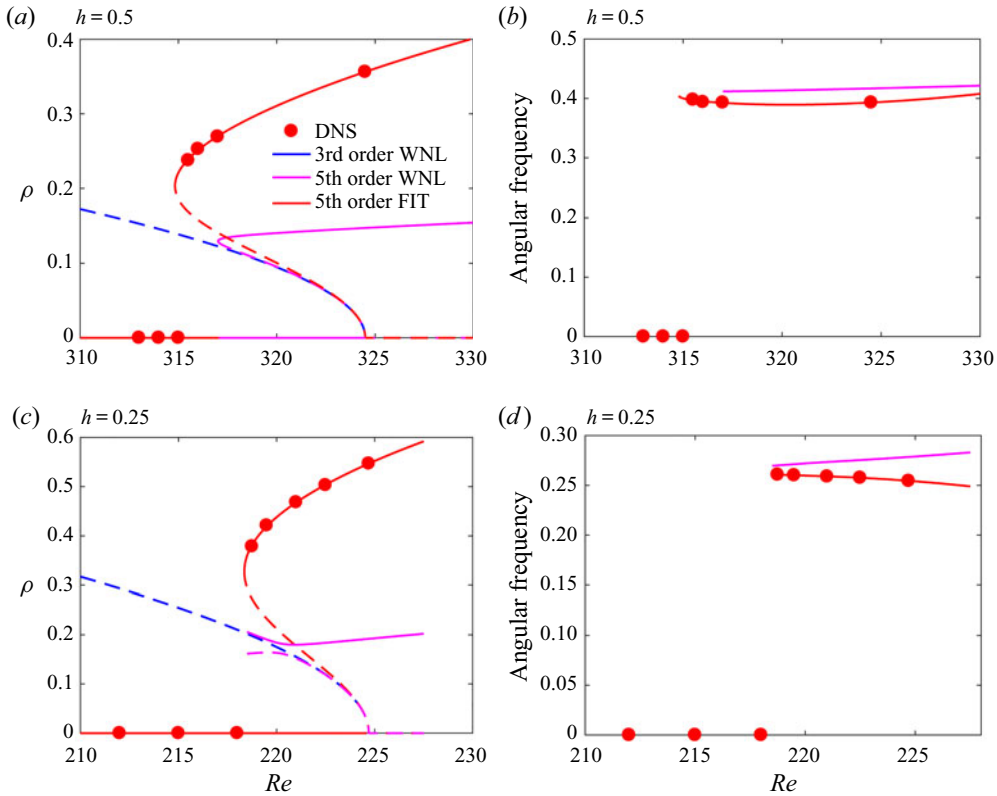


Figure 18. Amplitudes and frequencies of the third- and fifth-order WNL analyses as well as the fifth-order amplitude equation obtained by fitting the DNS data at $h = 0.5$ and $h = 0.25$ and for $S = 1.0$.

with

$$\lambda_2 = \langle \nabla_1 \mathbf{u}_{3\delta A_1} \cdot \mathbf{u}_{2\delta} + \nabla \mathbf{u}_{2\delta} \cdot \mathbf{u}_{3\delta A_1} + \nabla_1^2 \mathbf{u}_{3\delta A_1} + \lambda \mathbf{u}_{3\delta A_1}, \mathbf{u}_{1A_1}^\dagger \rangle, \quad (\text{B40})$$

$$\begin{aligned} \mu_2 = & \langle \nabla_1 \mathbf{u}_{1A_1} \cdot \mathbf{u}_{4|A_1|^2} + \nabla \mathbf{u}_{4|A_1|^2} \cdot \mathbf{u}_{1A_1} + \nabla_1 \mathbf{u}_{1A_1}^* \cdot \mathbf{u}_{4A_1^2} + \nabla \mathbf{u}_{4A_1^2} \cdot \mathbf{u}_{1A_1}^* \\ & + \nabla \mathbf{u}_{2\delta} \cdot \mathbf{u}_{3A_1|A_1|^2} + \nabla \mathbf{u}_{3A_1|A_1|^2} \cdot \mathbf{u}_{2\delta} + \nabla \mathbf{u}_{3\delta A_1}^* \cdot \mathbf{u}_{2A_1^2} + \nabla \mathbf{u}_{2A_1^2} \cdot \mathbf{u}_{3\delta A_1}^* \\ & + \nabla \mathbf{u}_{2|A_1|^2} \cdot \mathbf{u}_{3\delta A_1} + \nabla \mathbf{u}_{3\delta A_1} \cdot \mathbf{u}_{2|A_1|^2} + \nabla_1^2 \mathbf{u}_{3\delta A_1} + \alpha \mathbf{u}_{3\delta A_1}^* \\ & + (2\lambda + \lambda^*) \mathbf{u}_{3A_1|A_1|^2}, \mathbf{u}_{1A_1}^\dagger \rangle, \end{aligned} \quad (\text{B41})$$

$$\begin{aligned} \gamma = & \langle \nabla_1 \mathbf{u}_{1A_1} \cdot \mathbf{u}_{4|A_1|^4} + \nabla \mathbf{u}_{4|A_1|^4} \cdot \mathbf{u}_{1A_1} + \nabla_1 \mathbf{u}_{1A_1}^* \cdot \mathbf{u}_{4A_1^2|A_1|^2} + \nabla \mathbf{u}_{4A_1^2|A_1|^2} \cdot \mathbf{u}_{1A_1}^* \\ & + \nabla \mathbf{u}_{2|A_1|^2} \cdot \mathbf{u}_{3A_1|A_1|^2} + \nabla \mathbf{u}_{3A_1|A_1|^2} \cdot \mathbf{u}_{2|A_1|^2} + \nabla \mathbf{u}_{3A_1^*|A_1|^2} \cdot \mathbf{u}_{2A_1^2} \\ & + \nabla \mathbf{u}_{2A_1^2} \cdot \mathbf{u}_{3A_1^*|A_1|^2} + \nabla \mathbf{u}_{2A_1^2} \cdot \mathbf{u}_{3A_1^3} + \nabla \mathbf{u}_{3A_1^3} \cdot \mathbf{u}_{2A_1^2} + \nabla_1^2 \mathbf{u}_{3\delta A_1} \\ & + (2\alpha + \alpha^*) \mathbf{u}_{3A_1|A_1|^2}, \mathbf{u}_{1A_1}^\dagger \rangle, \end{aligned} \quad (\text{B42})$$

defining λ_2 , μ_2 and γ , the fifth-order coefficients. The numerical values of these coefficients for the present configuration are reported in [table 6](#). The amplitude equation is written in polar coordinates assuming $a = \rho e^{i\phi}$. Plugging this definition into [\(B39\)](#) and

separating the real part from the imaginary part yields to

$$\rho' = \epsilon^2(\lambda_{1r} + \epsilon^2\lambda_{2r})\rho + (\mu_{1r} + \epsilon^2\mu_{2r})\rho^3 + \gamma\rho^5, \quad (\text{B43})$$

$$\phi' = \epsilon^2(\lambda_{1i} + \epsilon^2\lambda_{2i}) + (\mu_{1i} + \epsilon^2\mu_{2i})\rho^2 + \gamma\rho^4. \quad (\text{B44})$$

The final solution is: $\mathbf{q} = \mathbf{q}_0 + \rho e^{i\phi} \mathbf{q}_1 e^{i\theta - i\omega ct} + \epsilon^2 \mathbf{q}_2 + \epsilon^3 \mathbf{q}_3 + h.o.t..$ This solution is displayed in figure 18 with the coefficients given in table 6.

REFERENCES

- ALEKSEENKO, S.V., KUIBIN, P.A., OKULOV, V.L. & SHTORK, S.I. 1999 Helical vortices in swirl flow. *J. Fluid Mech.* **382**, 195–243.
- ALTHAUS, W., KRAUSE, E., HOFHAUS, J. & WEIMER, M. 1994 Vortex breakdown: transition between bubble- and spiral-type breakdown. *Meccanica* **29** (4), 373–382.
- BENJAMIN, T.B. 1962 Theory of the vortex breakdown phenomenon. *J. Fluid Mech.* **14** (4), 593–629.
- BILLANT, P., CHOMAZ, J.-M. & HUERRE, P. 1998 Experimental study of vortex breakdown in swirling jets. *J. Fluid Mech.* **376**, 183–219.
- CITRO, V., TCHOUFAG, J., FABRE, D., GIANNETTI, F. & LUCHINI, P. 2016 Linear stability and weakly nonlinear analysis of the flow past rotating spheres. *J. Fluid Mech.* **807**, 62–86.
- DELBENDE, I., CHOMAZ, J.-C. & HUERRE, P. 1998 Absolute/convective instabilities in the batchelor vortex: a numerical study of the linear impulse response. *J. Fluid Mech.* **355**, 229–254.
- DELERY, J.M. 1994 Aspects of vortex breakdown. *Prog. Aerosp. Sci.* **30** (1), 1–59.
- DUSEK, J., GAL, P.L. & FRAUNTIÉ, P. 1994 A numerical and theoretical study of the first Hopf bifurcation in a cylinder wake. *J. Fluid Mech.* **264**, 59–80.
- ESCUDIER, M.P. 1984 Observations of the flow produced in a cylindrical container by a rotating endwall. *Exp. Fluids* **2** (4), 189–196.
- FERNANDEZ-FERIA, R. 1996 Viscous and inviscid instabilities of non-parallel self-similar axisymmetric vortex cores. *J. Fluid Mech.* **323**, 339–365.
- FISCHER, P.F., LOTTES, J.W. & KERKEMEIER, S.G. 2008 nek5000. Available at: <http://nek5000.mcs.anl.gov>.
- FUJIMURA, K. 1991 Methods of centre manifold and multiple scales in the theory of weakly nonlinear stability for fluid motions. *Proc. R. Soc. Lond. A* **434**, 719–733.
- GALLAIRE, F. & CHOMAZ, J.M. 2003 Instability mechanisms in swirling flows. *Phys. Fluids* **15** (9), 2622–2639.
- GALLAIRE, F., RUIH, M., MEIBURG, E., CHOMAZ, J.-M. & HUERRE, P. 2006 Spiral vortex breakdown as a global mode. *J. Fluid Mech.* **549**, 71–80.
- HALL, M.G. 1972 Vortex breakdown. *Annu. Rev. Fluid Mech.* **4**, 195–218.
- HEATON, C.J., NICHOLS, J.W. & SCHMID, P.J. 2009 Global linear stability of the non-parallel batchelor vortex. *J. Fluid Mech.* **629**, 139–160.
- HECHT, F. 2012 New development in freefem++. *J. Numer. Maths* **20** (3–4), 251–265.
- HERRADA, M.A. & FERNANDEZ-FERIA, R. 2006 On the development of three-dimensional vortex breakdown in cylindrical regions. *Phys. Fluids* **18** (8), 084105.
- JOCHMANN, P., SINIGERSKY, A., HEHLE, M., SCHÄFER, O., KOCH, R. & BAUER, H.-J. 2006 Numerical simulation of a precessing vortex breakdown. *Intl J. Heat Fluid Flow* **27** (2), 192–203.
- JONES, M.C., HOURIGAN, K. & THOMPSON, M.C. 2015 A study of the geometry and parameter dependence of vortex breakdown. *Phys. Fluids* **27** (4), 044102.
- KRAUSE, E. 1985 A contribution to the problem of vortex breakdown. *Comput. Fluids* **13** (3), 375–381.
- LAMBOURNE, N.C. & BRYER, D.W. 1962 The bursting of leading-edge vortices – some observations and discussion of the phenomenon. *Aero. Res. Council. R&M* **3292**, 1–35.
- LEIBOVICH, S. 1978 The structure of the vortex breakdown. *Annu. Rev. Fluid Mech.* **10**, 221–246.
- LEIBOVICH, S. & STEWARTSON, K. 1983 A sufficient condition for the instability of columnar vortices. *J. Fluid Mech.* **126**, 335–356.
- LOPEZ, J.M. 1994 On the bifurcation structure of axisymmetric vortex breakdown in a constricted pipe. *Phys. Fluids* **6** (11), 3683–3693.
- LOPEZ, J.M. 2006 Rotating and modulated rotating waves in transitions of an enclosed swirling flow. *J. Fluid Mech.* **553**, 323–346.
- LUCCA-NEGRO, O. & O'DOHERTY, T. 2001 Vortex breakdown: a review. *Prog. Energy Combust. Sci.* **27**, 431–481.

Vortex impingement onto an axisymmetric obstacle

- MAGER, A. 1972 Dissipation and breakdown of a wing-tip vortex. *J. Fluid Mech.* **55** (4), 609–628.
- MATTNER, T.W., JOUBERT, P.N. & CHONG, M.S. 2002 Vortical flow. Part 1. Flow through a constant-diameter pipe. *J. Fluid Mech.* **463**, 259–291.
- MELIGA, P. & GALLAIRE, F. 2011 Control of axisymmetric vortex breakdown in a constricted pipe: nonlinear steady states and weakly nonlinear asymptotic expansions. *Phys. Fluids* **23** (8), 084102.
- MELIGA, P., GALLAIRE, F. & CHOMAZ, J.-M. 2012 A weakly nonlinear mechanism for mode selection in swirling jets. *J. Fluid Mech.* **699**, 216–262.
- MOISE, P. & MATHEW, J. 2019 Bubble and conical forms of vortex breakdown in swirling jets. *J. Fluid Mech.* **873**, 322–357.
- NAUMOV, I.V. & PODOLSKAYA, I.YU. 2017 Topology of vortex breakdown in closed polygonal containers. *J. Fluid Mech.* **820**, 263–283.
- NISHI, M., MATSUNAGA, S., KUBOTA, T. & SENOO, A. 1984 Surging characteristics of conical and elbow-type draft tubes. In *Proceedings of the 12th IAHR Symposium on Hydraulic Machinery and System, Stirling, Scotland*.
- OBERLEITHNER, K., SIEBER, M., NAYERI, C.N., PETZ, C., HEGE, H.-C., NOACK, R.R. & WYGNANSKI, I. 2011 Three-dimensional coherent structures in a swirling jet undergoing vortex breakdown: stability analysis and empirical mode construction. *J. Fluid Mech.* **679**, 383–414.
- OBERLEITHNER, K., STÖHR, M., IM, S.H., ARNDT, C.M. & STEINBERG, A.M. 2015 Formation and flame-induced suppression of the precessing vortex core in a swirl combustor: experiments and linear stability analysis. *Combust. Flame* **162** (8), 3100–3114.
- OKULOV, V.L. 2004 On the stability of multiple helical vortices. *J. Fluid Mech.* **521**, 319–342.
- PAGAN, D. & BENAY, R. 1987 Vortex breakdown induced by an adverse pressure gradient – experimental and numerical approaches. In *5th Applied Aerodynamics Conference, AIAA meeting Monterey, CA*. Available at: <https://doi.org/10.2514/6.1987-2478>.
- PASCHE, S., AVELLAN, F. & GALLAIRE, F. 2017 Part load vortex rope as a global unstable mode. *Trans. ASME: J. Fluids Engng* **139** (5), 051102.
- PASCHE, S., AVELLAN, F. & GALLAIRE, F. 2018a Onset of chaos in helical vortex breakdown at low Reynolds number. *Phys. Rev. Fluids* **3**, 064701.
- PASCHE, S., GALLAIRE, F. & AVELLAN, F. 2018b Predictive control of spiral vortex breakdown. *J. Fluid Mech.* **842**, 58–86.
- PASCHE, S., GALLAIRE, F. & AVELLAN, F. 2019 Origin of the synchronous pressure fluctuations in the draft tube of Francis turbines operating at part load conditions. *J. Fluids Struct.* **86**, 13–33.
- PASCHE, S., GALLAIRE, F., DREYER, M. & FARHAT, M. 2014 Obstacle-induced spiral vortex breakdown. *Exp. Fluids* **55**, 1784.
- PASCHEREIT, C.O., FLOHR, P. & GUTMARK, E.J. 2002 Combustion control by vortex breakdown stabilization. *Trans. ASME: J. Turbomach.* **128**, 679–688.
- QADRI, U.A., MISTRY, D. & JUNIPER, M.P. 2013 Structural sensitivity of spiral vortex breakdown. *J. Fluid Mech.* **720**, 558–581.
- ROCKWELL, D. 1998 Vortex-body interactions. *Annu. Rev. Fluid Mech.* **30** (1), 199–229.
- RUIH, M.R., CHEN, P., MEIBURG, E. & MAXWORTHY, T. 2003 Three-dimensional vortex breakdown in swirling jets and wakes: direct numerical simulation. *J. Fluid Mech.* **486**, 331–378.
- RUSAK, Z., JUDD, K.P. & WANG, S. 1997 The effect of small pipe divergence on near critical swirling flows. *Phys. Fluids* **9** (8), 2273–2285.
- RUSAK, Z., WHITING, C.H. & WANG, S. 1998 Axisymmetric breakdown of a q -vortex in a pipe. *AIAA J.* **36** (10), 1848–1853.
- RUSAK, Z., ZHANG, Y., LEE, H. & WANG, S. 2017 Swirling flow states in finite-length diverging or contracting circular pipes. *J. Fluid Mech.* **819**, 678–712.
- SALINGER, A.G., BURROUGHS, E.A., PAWLOWSKI, R.P., PHIPPS, E.T. & ROMERO, L.A. 2005 Bifurcation tracking algorithms and software for large scale applications. *Intl J. Bifurcation Chaos* **15** (03), 1015–1032.
- SARPKAYA, T. 1971 On stationary and travelling vortex breakdowns. *J. Fluid Mech.* **45** (3), 545–559.
- SARPKAYA, T. 1974 Effect of the adverse pressure gradient on vortex breakdown. *AIAA J.* **12** (5), 602–607.
- SERRE, E. & BONToux, P. 2002 Vortex breakdown in a three-dimensional swirling flow. *J. Fluid Mech.* **459**, 347–370.
- SHTERN, V. & HUSSAIN, F. 1999 Collapse, symmetry breaking, and hysteresis in swirling flows. *Annu. Rev. Fluid Mech.* **31** (1), 537–566.
- SIPP, D. & LEBEDEV, A. 2007 Global stability of base and mean flows: a general approach and its applications to cylinder and open cavity flows. *J. Fluid Mech.* **593**, 333–358.

- SORENSEN, J.N., NAUMOV, I.V. & OKULOV, V.L. 2011 Multiple helical modes of vortex breakdown. *J. Fluid Mech.* **683**, 430–441.
- SOTIROPOULOS, F., VENTIKOS, Y. & LACKEY, T.C. 2001 Chaotic advection in three-dimensional stationary vortex-breakdown bubbles: šil'nikov's chaos and the devil's staircase. *J. Fluid Mech.* **444**, 257–297.
- SPALL, R.E., GATSKI, T.B. & ASH, R.L. 1990 The structure and dynamics of bubble-type vortex breakdown. *Proc. R. Soc. Lond. A* **429**, 613–637.
- SPOHN, A., MOIRY, M. & HOPFINGER, E.J. 1993 Observations of vortex breakdown in an open cylindrical container with a rotating bottom. *Exp. Fluids* **14**, 70.
- SUSAN-RESIGA, R., VU, T.C., MUNTEAN, S., CIOCAN, G.D. & NENNEMANN, B. 2006 Jet control of the draft tube vortex rope in Francis turbines at partial discharge. In *Proceedings of the 23th IAHR Symposium on Hydraulic Machinery and Systems, Yokohama, Japan*.
- TAMMISOLA, O. & JUNIPER, M.P. 2016 Coherent structures in a swirl injector at $Re = 4800$ by nonlinear simulations and linear global modes. *J. Fluid Mech.* **792**, 620–657.
- VIOLA, F. 2016 Resonance in swirling wakes and sloshing waves non-normal and sublinear effects. Thesis, EPFL.
- WANG, S. & RUSAK, Z. 1997 The dynamics of a swirling flow in a pipe and transition to axisymmetric vortex breakdown. *J. Fluid Mech.* **340**, 177–223.